

Synergistic antiviral effects of structure-guided peptides and a mutagenic base analog on SARS-CoV-2 replication

Sergio Ortega Del Campo,¹ Gregorio Joaquín Fernández Ballester,² Clara Blanes Mira,³ Víctor Guirado Osorio,⁴ Luis Díaz Martínez,⁴ Ana Isabel de Ávila,⁵ María Eugenia Soria,^{5,6} Brenda Martínez-González,^{5,6} Francisco José Villena González,¹ Josefa Gómez-Maldonado,⁷ María Isabel Viciano Ramos,^{8,9} Encarnación Clavijo Frutos,^{8,9} Jesús L. Santos González,^{8,9} Ugo Bastolla,⁵ Celia Perales,^{5,6} Esteban Domingo,⁵ Enrique Víguera,¹ Ana María Fernández Escamilla,² Ana Grande Pérez¹

AUTHOR AFFILIATIONS See affiliation list on p. 19.

ABSTRACT The limited durability of vaccine protection and the rapid emergence of SARS-CoV-2 variants highlight the need for antiviral strategies that extend beyond vaccination and conventional small-molecule inhibitors. Here, we explored a dual approach combining structure-guided peptides predicted to interfere with the viral replication complex with lethal mutagenesis to limit SARS-CoV-2 replication. Using the crystallographic interfaces of nsp10 with nsp14 and nsp16, we designed short inhibitory peptides predicted to interact with the viral proofreading and RNA-capping machinery. In parallel, the mutagenic analog 5-fluorouracil was evaluated to determine its effect on SARS-CoV-2 in Vero E6 cells. Peptides P1 and P6 exhibited potent antiviral activity with minimal cytotoxicity, whereas 5-FU reduced specific infectivity without impairing genome replication. Combined treatment with 5-FU and peptide P1 resulted in $>10^4$ -fold reduction in infectious virus, achieving near-complete loss of infectivity at non-cytotoxic concentrations. Next-generation sequencing revealed that dual treatment increased mutation frequency, altered mutant spectra, and decreased genome stability, consistent with progression toward error catastrophe. Principal component analysis confirmed that combined treatment generated mutant spectra distinct from either monotherapy. These findings are consistent with a dual antiviral strategy in which structure-guided peptides designed to interact with components of the SARS-CoV-2 replication complex act in combination with lethal mutagenesis to produce a synergistic interaction between these two complementary processes. This integrated approach suggests a potential broad-spectrum antiviral strategy with applicability to other coronaviruses.

KEYWORDS SARS-CoV-2, ExoN activity, MTase activity, nsp10, 5-fluorouracil, peptide design, drug combination, synergism, mutant spectra, lethal mutagenesis

Although vaccination remains a cornerstone for controlling the SARS-CoV-2 pandemic, the emergence of new variants has raised concerns about reduced vaccine effectiveness. Recent variants have shown lower sensitivity to vaccine-induced neutralization (1–6). The high mutation rate inherent to RNA virus replication gives rise to mutant swarms or viral quasispecies (7, 8).

A key consequence of quasispecies dynamics is the rapid emergence of drug- and antibody-resistant mutants (9, 10). These minority variants may harbor advantageous mutations, become dominant within viral populations, and ultimately undermine conventional antiviral strategies (11–14). Therefore, novel antiviral strategies are urgently needed to complement vaccination, particularly against emerging variants capable of immune escape.

Building on viral mutation dynamics and quasispecies theory, lethal mutagenesis has been proposed as an antiviral strategy aimed at driving viruses to extinction

Editor Zhaohui Qian, Chinese Academy of Medical Sciences & Peking Union Medical College, Beijing, China

Address correspondence to Ana Grande Pérez, agrande@uma.es, or Ana María Fernández Escamilla, ana.fernandez@umh.es.

A.G.P., E.V., A.M.F.E., G.J.F.B., C.B.M., S.O.D.C., J.L.S.G., M.I.V.R., and E.C.F. are inventors on the Spanish patent application ES 3007932 A1 ("5-fluorouracil as an antiviral agent against viruses of the Coronaviridae family"), which is currently under examination by the Spanish Patent and Trademark Office (OEPM). This patent application covers aspects related to the findings reported in this manuscript. The other authors report no disclosures.

See the funding table on p. 20.

Received 12 December 2025

Accepted 29 March 2026

Published 27 April 2026

Copyright © 2026 Ortega Del Campo et al. This is an open-access article distributed under the terms of the [Creative Commons Attribution 4.0 International license](https://creativecommons.org/licenses/by/4.0/).

by increasing the replication error rate beyond a tolerable threshold, promoting the accumulation of deleterious mutations and loss of infectivity (15, 16). This principle has been validated using base and nucleoside analogs that enhance mutagenesis and cause viral extinction in several animal and plant RNA viruses (17–20). Among these compounds, the nucleoside analog β -D-*N*⁴-hydroxycytidine (NHC; molnupiravir) induces lethal mutagenesis in SARS-CoV-2 and effectively inhibits infection (21, 22). More recently, the synergistic combination of remdesivir and ribavirin, based on lethal mutagenesis, has been explored for SARS-CoV-2 inhibition (23).

In addition to increasing mutation rates, analogs can reshape viral genome composition, including dinucleotide usage patterns. RNA viruses evolve under compositional constraints that shape genome structure, including marked suppression of CpG and UpA dinucleotides (24, 25). Reduced CpG content is believed to facilitate evasion of the antiviral zinc-finger protein ZAP, which binds CpG dinucleotides and directs them toward degradation via cofactors such as KHNYN (26–28). SARS-CoV-2 exhibits extreme CpG deficiency, lower than that of other betacoronaviruses, suggesting strong selective pressure to evade ZAP- and APOBEC-mediated innate immune pathways (29–32).

However, the 3'→5' exonuclease proofreading activity of coronaviruses (33) may counteract the mutagenic effects of nucleoside analogs (34). To overcome this barrier, antiviral peptides designed to target SARS-CoV-2 replication proteins have emerged as a promising complementary strategy (35–37). One particularly attractive target is nsp10, a multifunctional cofactor that interacts with nsp14 and nsp16, modulating both the exonuclease activity of nsp14 and the 2'-O-methyltransferase (2'-O-MTase) activity of nsp16 (38, 39). Nsp10 is highly conserved among coronaviruses due to its essential roles in replication fidelity and genome maintenance (40, 41). Consequently, the binding interfaces of the nsp10-nsp14 and nsp10-nsp16 complexes represent promising targets for structure-guided inhibitory peptides (42–46).

The objective of this study was to design and evaluate a combinatorial antiviral therapy that integrates mutagenic and peptide-based inhibitors against SARS-CoV-2. We selected 5-fluorouracil (5-FU) as the mutagen, based on computational predictions of its effects on the Wuhan-Hu-1 genome and prior evidence of its antiviral activity in other RNA viruses (18, 20, 47). For peptide design, we used crystal structures of SARS-CoV and SARS-CoV-2 to identify the nsp10-nsp16 and nsp10-nsp14 interfaces and selected peptide fragments based on length, secondary structure, and predicted binding energy. Peptides were ranked according to interaction energy and intramolecular stability and were predicted to interact with nsp14 and nsp16, potentially interfering with the formation of functional heterodimers required for viral replication (42, 43, 46). We then evaluated their cytotoxicity and antiviral efficacy, individually and in combination with 5-FU, in Vero E6 cells infected with the Omicron BA.1.17 variant. Viral infectivity was quantified by plaque assay, and viral RNA, by RT-qPCR. Selected samples were subsequently analyzed by next-generation sequencing (NGS) to characterize mutant spectra and genetic diversity.

MATERIALS AND METHODS

Computational prediction of the effect of lethal mutagenesis on SARS-CoV-2

A computational framework was used to predict the effect of different types of base substitutions on SARS-CoV-2 replicative fitness. These analyses simulated the potential action of nucleoside analogs by evaluating their expected impact on dinucleotide frequencies and protein stability.

Estimation of dinucleotide effects

The contribution of each dinucleotide to viral fitness was estimated by comparing its observed frequency in the viral genome with the expected frequency based on overall nucleotide composition, using the following formula:

$$\text{Fitness (XY)} = \log\left(\frac{\text{freq}_{\text{observed}}(\text{XY})}{\text{freq}_{\text{expected}}(\text{XY})}\right)$$

Calculations were performed using the Wuhan-Hu-1 reference genome (GenBank accession [NC_045512.2](#)). The estimated impact of mutations on fitness was derived from the expected effect of each substitution type on dinucleotide frequency. This analysis is inherently linked to both the number and distribution of mutations and dinucleotides along the genome.

Estimation of mutational costs

The effects of amino acid substitutions on protein stability were predicted as a proxy for fitness using the DeltaGREM method (48). This model estimates the protein folding free energy, ΔG , as the difference between the free energy of the native state, estimated through the contact free energy parameters developed in a previous study (49), and the free energy of compact misfolded conformations, estimated using a contact-based model developed (50) in analogy with the Random Energy Model (51). Fitness was estimated from these values using the following equation:

$$\text{Fitness} = \frac{\exp\left(\frac{-\Delta G}{RT}\right)}{1 + \exp\left(\frac{-\Delta G}{RT}\right)}$$

For all possible amino acid changes in each viral protein, DeltaGREM calculates the corresponding change in folding free energy $\Delta\Delta G$. The program was applied as described by de la Higuera et al. (52) to estimate the mutational load produced by different mutational spectra.

We analyzed all SARS-CoV-2 proteins with experimentally resolved structures in the Protein Data Bank (PDB) together with their corresponding nucleotide sequences. For each protein, we predicted the average value of $\Delta\Delta G$ for all possible mutations at the nucleotide level and evaluated the corresponding changes at the amino acid level. This enabled the prediction of the structural and stability impact of every type of mutation at the nucleotide level.

Computational peptide design

Visualization and identification of interacting regions

Crystal structures of SARS-CoV-2 nsp10-nsp14 (PDB [7DIY](#)) and nsp10-nsp16 (PDB [6W4H](#)) complexes were retrieved from the RCSB PDB (<https://www.rcsb.org/>). Contact regions were identified by visual inspection using PyMOL v3 (The PyMOL Molecular Graphics System, Version 3.0 Schrödinger, LLC; <https://www.pymol.org/>). Nsp10 was fragmented into 9–12 amino acid segments used as ligand candidates, while nsp14 or nsp16 served as receptors for computational modeling. The resulting complexes were isolated for sequence optimization and energy evaluation.

A conservation analysis of the interaction interfaces was also performed. Protein sequences of nsp10, nsp14, and nsp16 from representative coronaviruses were retrieved, and genomic regions were extracted from annotated reference genomes. Multiple sequence alignments were generated with MAFFT using default parameters (53). Contact residues of the nsp10-nsp14 and nsp10-nsp16 complexes were then analyzed, and sequence logos visualizing positional conservation and variability were produced using WebLogo (<https://weblogo.threplusone.com/create.cgi>).

Interaction energy calculations

Interaction energies were computed using FoldX v5.0 (<https://foldxsuite.crg.eu/>), which estimates contributions from electrostatic interactions, hydrogen bonds, disulfide bridges, van der Waals forces, dipole interactions, solvation, and entropic factors. The

sum of these contributions yielded total estimated interaction energy, and complexes with the most favorable (most negative) values were selected for further optimization.

For the nsp10-nsp14 interface, the nsp10 peptide 39-TNCVKMLCT-47 (9 aa) was chosen as the ligand, and the full-length nsp14 was used as the receptor (Fig. 1A and B). The same region was later considered within the nsp10-nsp16 complex to evaluate its potential dual-target interaction *in silico* (Fig. 1E and F). An additional contact region within nsp10, corresponding to helix α 1 (11-STVLSFCAFAVD-22), was also considered an alternative binding motif toward nsp14 (Fig. 1C and D).

Selection of optimal peptide sequences

Bound nsp10 peptides were optimized in FoldX by considering the local amino acid environment (56). Position-specific scoring matrices were generated and visualized as color-coded maps to identify residues contributing most to binding affinity (Fig. S1).

Two iterative rounds of sequence optimization were performed, combining the best-scoring residues per position. Positions were classified as buried, semi-buried, or exposed, generating 1,000–5,000 variants per round and ranked by predicted binding energy. Round 1 prioritized buried and semi-buried positions, typically improving $\Delta G_{\text{binding}}$ by ≈ 3 kcal/mol relative to the wild-type fragment. Round 2 refined exposed and key positions and produced an additional ≈ 1 kcal/mol improvement on average.

Selection criteria included predicted interaction energy, hydrophobic content, and sequence similarity to the native fragment. The top eight optimized peptides (9–12 aa) were selected for *in vitro* assays. To improve intracellular stability, N-terminal acetylation and C-terminal amidation were introduced.

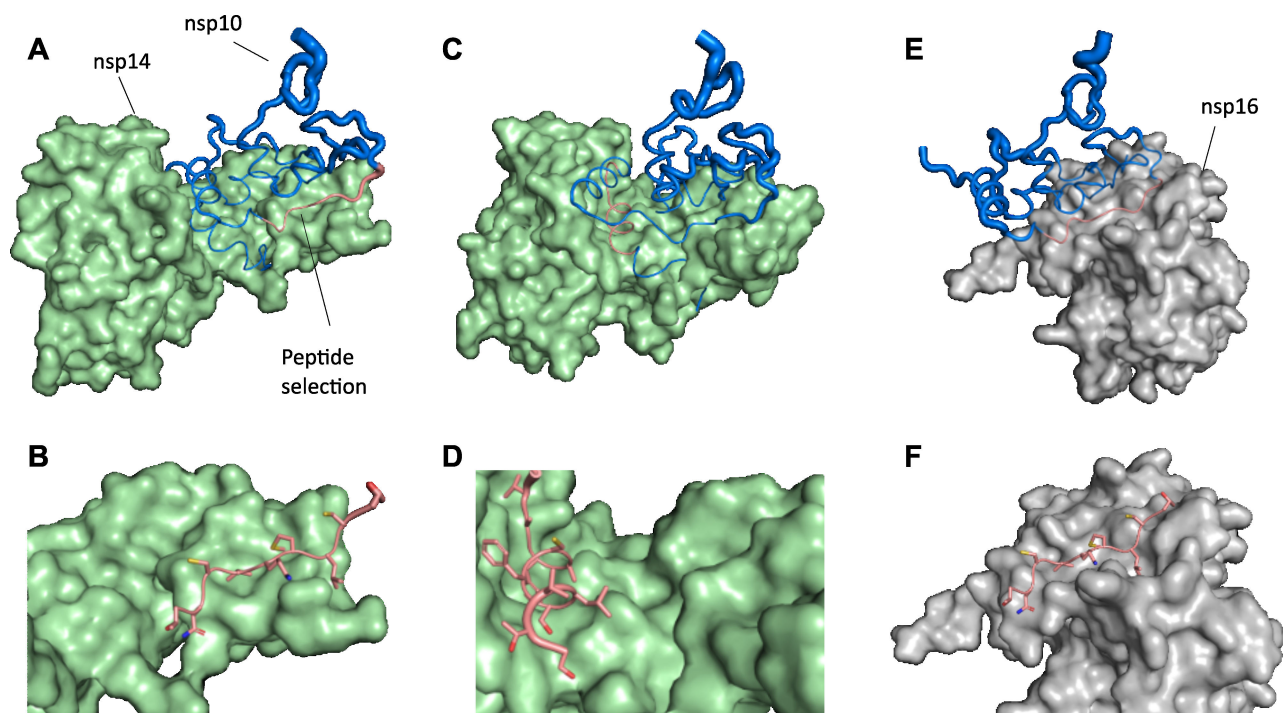


FIG 1 Structural basis for the design of inhibitory peptides designed to target the SARS-CoV-2 nsp10-nsp14 and nsp10-nsp16 interfaces, based on computational modeling. (A) Interface of nsp14 exoribonuclease (green surface) contacting nsp10 (blue cartoon). The nsp10 segment 39-TNCVKMLCT-47 used as a template for peptide design is shown in salmon. (B) Close-up of the nsp14-peptide complex after deleting the remaining nsp10 residues, showing the region used for binding-energy calculation. (C) Alternative contact region in nsp10 corresponding to helix α 1 (11-STVLSFCAFAVD-22; salmon), considered an additional nsp14-binding motif. (D) Structural context of helix α 1 within nsp10, highlighting its orientation and interaction surface. (E) Interaction between nsp16 O-methyltransferase (gray surface) and nsp10 (blue), showing that the same 39-TNCVKMLCT-47 region (salmon) contributes to binding. (F) Close-up of the nsp16-peptide complex used for energy scoring. Structures were derived from the SARS-CoV-2 nsp14 ExonN complex (54) and the nsp16 O-MTase complex (55). These structural elements were used as input for computational design and optimization of candidate inhibitory peptides.

Cell culture assays

All experiments involving infectious SARS-CoV-2 were conducted in a BSL-3 facility at the Centro de Biología Molecular Severo Ochoa (CBM).

Cells and virus

Vero E6 cells (ATCC Cat# CRL-1586, RRID:CVCL_0574) were cultured in DMEM (Merck, Darmstadt, Germany) supplemented with 10% fetal bovine serum (Sigma, St. Louis, USA), 50 µg/mL gentamicin (Pan Biotech, Aidenbach, Germany), 4 mM L-glutamine (Merck), 0.2 µg/mL antifungal (Sigma), and 1% non-essential amino acids (Merck). Cell growth and maintenance followed established protocols (23, 57).

A nasopharyngeal swab from a severe COVID-19 patient (Hospital Clínico Virgen de la Victoria, Málaga) was used for virus isolation. Viral stocks were generated by infecting 3×10^6 Vero E6 cells at an MOI of 0.001 PFU/cell for 48 h at 37°C.

Drug exposure and cytotoxicity assays

Peptides were dissolved at 5 mg/mL in DMSO and stored at -80°C. 5-FU (Sigma, St. Louis, USA) was prepared as a 3 mM stock solution in DMEM. Peptide cytotoxicity was assessed using a concentration-response design, testing multiple concentrations up to a maximum of 70 µM, whereas 5-FU was evaluated over a wider concentration range. Cytotoxicity was assessed in 96-well plates (10^4 cells/well) after 72 h of exposure. MTT was added for 4 h, followed by 100 µL DMSO to dissolve the formazan crystals, and absorbance at 550 nm was measured to determine 50% cytotoxic concentration (CC₅₀); when no 50% reduction in cell viability was observed within the tested peptide concentration range, CC₅₀ values are reported as >70 µM.

Antiviral efficacy assays

Antiviral activity was assessed in six-well plates using virus passage 3. After 2 h of adsorption at 37°C, the inoculum was removed and replaced with a drug-containing medium. Infected cultures were harvested after 48 h.

Infectious titers (PFU/mL) were obtained by plaque assay, and IC₅₀ and therapeutic index (TI = CC₅₀/IC₅₀) were calculated.

Additionally, peptide internalization assays were performed in cells to evaluate the cellular uptake of peptides P1 and P7. These two peptides were selected as representative active candidates for assessing intracellular uptake. Vero E6 cells (6.25×10^5 per well) were seeded in six-well plates under standard culture conditions. GFP-labeled P1 and P7 were prepared from 5 mg/mL DMSO stocks and added directly to the cultures at final concentrations of 0.7, 7, and 70 µM. Cells were collected at 0, 6, 24, 36, and 48 h after peptide addition and examined by fluorescence microscopy. Three independent replicate wells were processed for each concentration and time point to ensure reproducibility and minimize potential phototoxicity during imaging.

Drug interactions were analyzed using the Chou-Talalay method with *CompuSyn* software, which computes combination indices (CI) to classify interactions as synergistic (CI < 1), additive (CI = 1), or antagonistic (CI > 1).

Characterization of mutant spectra

RNA extraction, amplification, and NGS

Supernatants from selected cultures (Table S1A) were processed for sequencing. Viral RNA was extracted using the QIAamp Viral RNA Mini Kit (Qiagen, Germany). Twelve overlapping ~3 kb amplicons covering the full SARS-CoV-2 genome were generated by RT-PCR using the Transcriptor One-Step RT-PCR Kit (Roche, Germany) (Table S1B). Amplicons were gel-purified with the QIAquick Gel Extraction Kit (Qiagen) and sequenced at the SCAI Ultrasequencing Unit (University of Málaga). Libraries were prepared with the Nextera XT DNA Library Prep kit (Illumina) and sequenced on an

Illumina NextSeq 550 platform (2 × 150 bp). Standard Illumina pipelines were used for base-calling and demultiplexing.

In parallel, the passage-3 viral stock used in the experiments was sequenced using the COVID-Seq protocol (Illumina), allowing variant assignment (Omicron variant, Pango BA.1.17, clade 21K) and the identification of characteristic mutations relative to the Wuhan-Hu-1 reference genome (NC_045512.2) (Fig. S2). The sequence has been deposited in GenBank under accession number PV483427.1.

Viral RNA quantification

Viral RNA was quantified by RT-qPCR using the LightCycler RNA Master SYBR Green Kit and LightCycler II system (Roche, Switzerland). Genome copy numbers were calculated from a standard curve generated with *in vitro*-transcribed RNA from the WA1/2020 SARS-CoV-2 strain. Specific infectivity (SI) was calculated as the ratio of infectious units (PFU) to total RNA genomes.

Bioinformatic analysis

Fastq files were processed following established pipelines (58, 59). Quality filtering was performed with FastQC and fastp (60). Clean reads were aligned to the SARS-CoV-2 reference genome PV483427.1 using BWA-MEM and processed with SAMtools. Minority variants were identified from each sample's consensus-aligned reads using LoFreq (frequency cutoff $\geq 0.1\%$) (61).

Genetic diversity metrics included mutation frequency, nucleotide diversity, and Shannon entropy. Statistical tests included Shapiro-Wilk for normality and Levene's test for variance homogeneity. Depending on the distribution, one-way ANOVA or Kruskal-Wallis tests were applied.

Mutation randomness was evaluated genome-wide and per ORF using a non-parametric runs test ($P < 0.05$). Dinucleotide frequencies were computed to assess compositional shifts in the mutant spectra.

RESULTS

Computational prediction of the effect of lethal mutagenesis on SARS-CoV-2

Dinucleotides with the lowest fitness scores were enriched in cytosine and guanine, particularly CpG, whose negative values indicated a detrimental impact on SARS-CoV-2 fitness. In contrast, CpU, UpG, and UpU displayed positive fitness values, suggesting that these dinucleotides favor viral replication. Mutational-load analysis revealed strong predicted fitness penalties for substitutions that increase disfavored dinucleotides. Among all mutation types, U→G, U→C, and A→G produced the highest mutational loads (Fig. 2), consistent with their tendency to increase G/C content.

When evaluating the fitness cost of each mutation across individual viral proteins, the most deleterious substitutions were U→G, U→A, and U→C (Table 1; Table S2). The predicted burden varied depending on protein identity and secondary structure. For example, in nsp10, U→G and U→A were most damaging, whereas in heterodimeric complexes (nsp10-nsp14 and nsp10-nsp16), as well as spike, G→U and C→U produced the strongest destabilizing effects.

Our results indicate that mutations that change uracil to any other nucleotide are especially detrimental for viral fitness. Mutations from other nucleotides to U, which increase hydrophobicity, are also detrimental, but less so. These computational results supported the selection of 5-FU, which predominantly induces U→C and A→G transitions (18, 62, 63), as a suitable mutagenic analog for experimental testing. Although not previously evaluated in SARS-CoV-2, 5-FU displays mutagenic activity in SARS-CoV (34, 45).

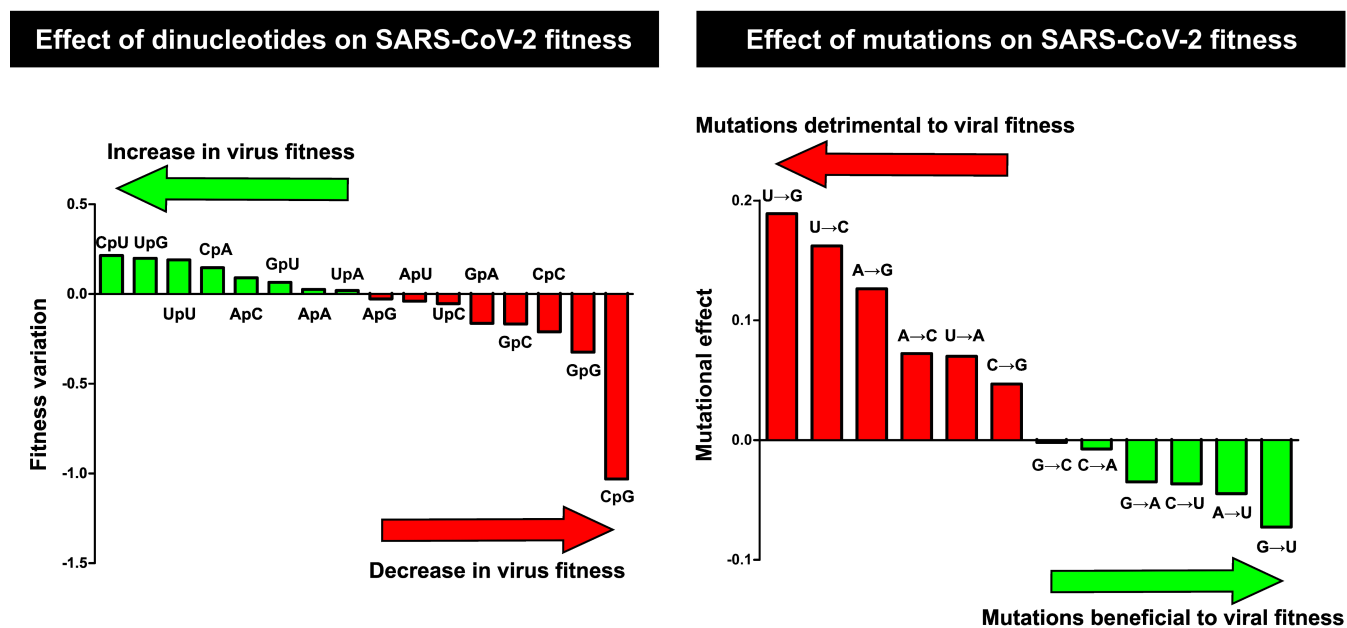


FIG 2 Left: Estimated effects of dinucleotides on SARS-CoV-2 fitness. Negative values indicate that the presence of these dinucleotides confers a fitness disadvantage, whereas positive values indicate a beneficial effect. Right: Predicted fitness effects of each mutation based on its expected impact on dinucleotide composition. Positive values indicate that the mutation increases unfavorable dinucleotides and/or reduces favorable dinucleotides. Negative values indicate the opposite pattern. Wuhan-Hu-1 (NC_045512.2) was used as the reference.

Computational peptide design

Using the structural templates defined in Methods (Fig. 1), two regions of nsp10, residues 39–47 and helix $\alpha 1$ (positions 11–22), were optimized as scaffolds for peptide inhibitors designed to interact with the nsp14 and nsp16 interfaces. These segments correspond to the principal interaction interfaces observed in crystallographic complexes.

For the nsp10-nsp14 interface, the native fragment 39-TNCVKMLCT-47 exhibited a predicted interaction energy of -9.63 kcal/mol. FoldX optimization produced peptide 39-QLQIYLMRK-47, with improved predicted interaction energy (-12.99 kcal/mol) and

TABLE 1 Effect of each substitution type on the fitness of SARS-CoV-2 proteins

Cost of mutations in the SARS-CoV-2 proteins		
Mutation ^a	nmut ^b	Mutation load ^c
U→G	5,194	0.0574
U→A	5,194	0.0544
U→C	5,194	0.0459
G→U	3,396	0.0451
A→U	4,963	0.0445
G→C	3,396	0.0311
C→U	3,214	0.0248
A→C	4,963	0.0210
G→A	3,396	0.0209
C→A	3,214	0.0148
C→G	3,214	0.0134
A→G	4,963	0.0075

^aThe mutations shown in the table are sorted according to their mutation load value in descending order.

^bnmut is the total number of nucleotide mutations.

^cMutation load = Total estimated fitness cost of mutations, measured by $\Delta\Delta G$ or change in the free energy of folding of a protein caused by a mutation; indicates whether the mutation stabilizes ($\Delta\Delta G < 0$) or destabilizes ($\Delta\Delta G > 0$) the protein.

reduced hydrophobic content, yielding a net charge of +2 compatible with the nsp14 electrostatic environment.

The $\alpha 1$ helix region (11-STVLSFCAFAVD-22) displayed a higher predicted intrinsic interaction energy (-15.45 kcal/mol). Two rounds of guided mutagenesis generated the optimized sequence 11-KIEKTFEYVMVR-22, with substantially improved predicted interaction energy (-26.27 kcal/mol). Phe16 and Val21 were retained due to their buried hydrophobic roles, consistent with their conservation across coronaviruses.

For nsp10-nsp16, optimization of the same 39–47 region yielded peptide 39-ELKIRMRWK-47, improving predicted interaction energy from -12.17 kcal/mol to -16.7 kcal/mol, driven by increased positive residues consistent with the nsp16 electrostatic landscape.

In total, eight peptides (9–12 aa) were selected for synthesis and biological evaluation (Table 2) based on (i) predicted interaction energy, (ii) physicochemical suitability, and (iii) complementarity to conserved interaction surfaces (Fig. 1; Fig. S1).

Comparative alignments of nsp10, nsp14, and nsp16 across the *Orthocoronavirinae* revealed strong conservation in the targeted interaction regions (Fig. 3). Conservation was highest in alpha- and beta-coronaviruses, moderate in gamma-coronaviruses, and lower in delta-coronaviruses (Table S3A through D), suggesting that these peptides may potentially interact with equivalent interfaces across genera, which is consistent with a potential pan-coronavirus applicability.

Culture-based experiments

Individual cytotoxicity and antiviral activity of peptides and 5-FU

Cytotoxicity assays in Vero E6 cells, performed using a concentration-response design, indicated that none of the peptides reached 50% cytotoxicity within the tested concentration range (up to $70 \mu\text{M}$), except P4 and P8, which caused mild cytotoxicity at the highest concentration tested (Fig. 3A; Table S4A). 5-FU showed minimal toxicity up to $100 \mu\text{M}$, but concentrations $\geq 400 \mu\text{M}$ reduced viability, reaching $<50\%$ at $800 \mu\text{M}$ (Fig. 3B). The $\text{CC}_{50} = 722.77 \mu\text{M}$ confirmed low cytotoxicity (Table 3).

Antiviral assays showed that several peptides reduced viral titers at $70 \mu\text{M}$ (Fig. 3C). The dose-response experiments were performed as an initial screening step to identify peptides with reproducible antiviral activity within the non-cytotoxic concentration range tested. The strongest inhibitor was P1 ($\text{IC}_{50} = 4.50 \mu\text{M}$; $\text{TI} > 15$). P3, P6, and P7 also showed measurable antiviral effects (Table 3). Although peptide P1 showed the clearest dose-dependent antiviral trend, the responses of P6 and P7 were less pronounced within the concentration range tested (Fig. S4). For peptides whose inhibitory activity did not reach 50% within the tested concentration range (up to $70 \mu\text{M}$), IC_{50} values are therefore reported as $\geq 70 \mu\text{M}$ and should be interpreted as approximate estimates. P4 and P8 were excluded due to cytotoxicity.

Based on these screening results, peptides P1, P6, and P7 were prioritized for further evaluation. Selection criteria included (i) reproducible reductions in viral infectivity

TABLE 2 Peptides designed on SARS-CoV-2 nsp10 and selected for *in vitro* assays

Peptide	Sequence	MW ^a	Net charge	Identity with WT (%)	Predicted interaction energy (kcal/mol)	Target protein ^b
P1	ELKIRMRWK	1,300.63	+3	1 (11%)	-16.70	nsp16
P2	ELKILMMWK	1,232.61	+1	1 (11%)	-16.97	nsp16
P3	QLQILMMKK	1,173.54	+2	1 (11%)	-13.03	nsp14
P4	ELKILLMKK	1,156.53	+2	0 (0%)	-12.89	nsp14
P5	QLQIIMMRK	1,201.56	+2	1 (11%)	-13.05	nsp14
P6	QLQIYLMRK	1,233.53	+2	0 (0%)	-12.99	nsp14
P7	KIEKTFEYVMVR	1,647.94	+1	2 (17%)	-26.27	nsp14
P8	KIERTFQYVMVR	1,674.97	+2	2 (17%)	-26.23	nsp14

^aMolecular weight.

^bPeptides P1–P6 were derived from the nsp10 region spanning residues 39–47 (TNCVKMLCT), which participate in both nsp10-nsp14 and nsp10-nsp16 interfaces. Although individually optimized toward one target based on structural modeling, potential cross-interaction with either protein cannot be excluded. Peptides P7 and P8 were derived from the helix $\alpha 1$ region of nsp10 (residues 11–22: STVLSFCAFAVD), primarily involved in the nsp10-nsp14 interaction.

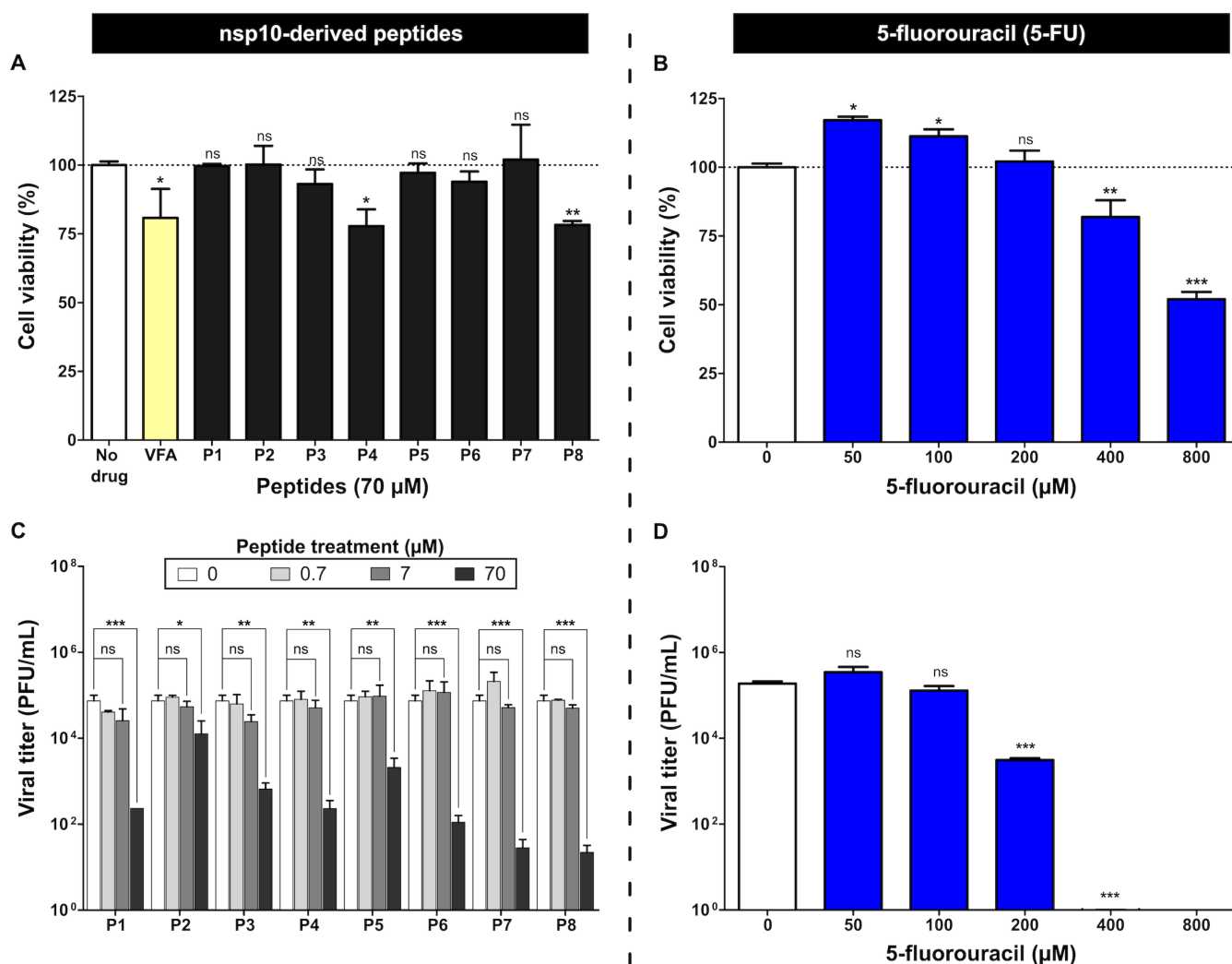


FIG 3 Initial screening of cytotoxicity and antiviral activity of peptides and 5-FU in Vero E6 cells. Cell viability (%) was determined by MTT assay after 72 h of exposure. Cytotoxicity was evaluated using a concentration-response design. (A) Cells treated with peptides P1–P8 at the highest concentration tested (70 μ M). A peptide targeting foot-and-mouth disease virus (VFA) was used as a control (Fig. S4). (B) Cells were treated with increasing concentrations of 5-FU. Complete concentration-response absorbance data and calculated percentages of viability and mortality are summarized in Table S4A. Viral infectivity was quantified by plaque assay (PFU/mL) 48 h post-infection. Dose-response analysis was used to identify peptides showing antiviral activity within the non-cytotoxic concentration range tested. (C) Cultures treated with peptides P1–P8 at increasing concentrations (0.7–70 μ M) to evaluate their effects on viral infectivity. (D) Cultures were treated with 5-FU at increasing concentrations. Complete viral titer data are summarized in Table S4B. Bars represent mean \pm SD ($n = 3$). Statistical analysis was performed by comparing each drug-treated condition with the untreated control. Asterisks indicate significant differences compared with the control (* $P < 0.05$; ** $P < 0.01$; *** $P < 0.001$); ns, not significant.

across independent experiments, (ii) absence of detectable cytotoxicity within the tested concentration range, (iii) representation of peptides derived from distinct nsp10 interaction regions, and (iv) potential complementarity with the mutagenic mechanism of 5-FU. P1 and P6 were selected for the main combination studies with 5-FU because they produced the most consistent antiviral reductions within the non-cytotoxic concentration range tested. P1 and P7 were used for cellular internalization assays, and P7 was additionally evaluated in exploratory low-dose combination experiments described below. This strategy allowed us to examine peptides with distinct antiviral behaviors while focusing the main combination analyses on the most consistent candidates.

Peptide internalization assays using GFP-conjugated P1 and P7 showed time- and concentration-dependent fluorescence signals consistent with cellular association and

TABLE 3 Cytotoxic (CC_{50}), inhibitory (IC_{50} , IC_{75}), and therapeutic index (TI) values for 5-FU and nsp10-derived peptides

Compound	CC_{50}^a (μM)	IC_{50}^b (μM)	IC_{75} (μM)	TI (CC_{50}/IC_{50})
5-FU	722.77	126.86	142.89	5.70
P1	> 70	4.50	12.10	> 15.56
P2	> 70	$\geq 70 \mu\text{M}$	154.87	> 0.64
P3	> 70	15.81	20.91	> 4.42
P4	> 70	41.89	54.57	> 1.67
P5	> 70	$\geq 70 \mu\text{M}$	87.96	> 1.07
P6	> 70	18.68	47.82	> 3.75
P7	> 70	17.07	38.21	> 4.10
P8	> 70	29.12	36.85	> 2.40

^a CC_{50} values are reported as >70 μM when no 50% cytotoxicity was reached within the tested peptide concentration range.

^b IC_{50} values that did not reach 50% inhibition within the tested concentration range (70 μM) should be interpreted as approximate estimates.

uptake. Fluorescence became detectable at 6 h for cultures treated with 7 μM and 70 μM , with P1 producing stronger and more homogeneous signals. Cell-associated fluorescence was broadly distributed throughout the cell area, with no granular or perinuclear pattern (Fig. S5). P7-treated cells showed weaker and more heterogeneous fluorescence, with maximal intensity at 24 h. At 0.7 μM , fluorescence was faint or absent for both peptides. No signal was detected in untreated control cells, and autofluorescence was negligible. Fluorescence intensity decreased by 36 h, particularly in P7-treated cultures. These observations indicate that both peptides, particularly P1, are capable of associating with cells and generating intracellular fluorescence signals in a time- and concentration-dependent manner.

In addition, the antiviral activity of 5-FU on SARS-CoV-2 was evaluated. Treatment with 5-FU alone produced no inhibition at $\leq 100 \mu\text{M}$ but caused a significant reduction at 200 μM and nearly complete loss of infectivity at $\geq 400 \mu\text{M}$ (Fig. 3D). The $IC_{50} = 126.86 \mu\text{M}$, well below the CC_{50} indicated effective inhibition of SARS-CoV-2 infectivity (Table 3).

Evaluation of drug combinations

We next examined whether peptides enhanced the antiviral activity of 5-FU. To evaluate the cytotoxicity and antiviral effects of peptide-5-FU combinations, peptides selected from the initial screening (P1, P6, and P7) were evaluated in combination with 5-FU, based on their reproducible antiviral activity and absence of cytotoxicity within the tested concentration range. Peptides P1, P6, and P7 (70 μM) were tested with increasing concentrations of 5-FU to assess whether combination treatment could enhance antiviral activity or modify cytotoxic profiles. Among these peptides, P7 showed the lowest combined cytotoxicity (Fig. 4A).

Based on the screening assays, peptides P1 and P6 were selected for the main antiviral evaluation in combination with 5-FU because they showed the most consistent antiviral reductions across the tested concentration range, whereas P7 was examined separately in a low-dose exploratory analysis. P1 and P6 were evaluated across the full concentration range of 5-FU tested in this study, whereas P7 was examined at lower doses to determine whether partial enhancement of antiviral activity could be detected near the IC_{50} range of both compounds. The combination of 5-FU with peptides P1 or P6 significantly reduced viral titers beyond the corresponding monotherapies. Notably, the 5-FU + P1 combination consistently yielded the strongest inhibition. At 500 μM 5-FU, no detectable infectivity remained when either peptide was present, indicating near-complete loss of infectivity (Fig. 4B).

To explore whether partial antiviral enhancement could be observed at lower concentrations, P7 was tested in combination with 5-FU using graded doses near the IC_{50} of each compound. Virus titers decreased progressively with increasing 5-FU

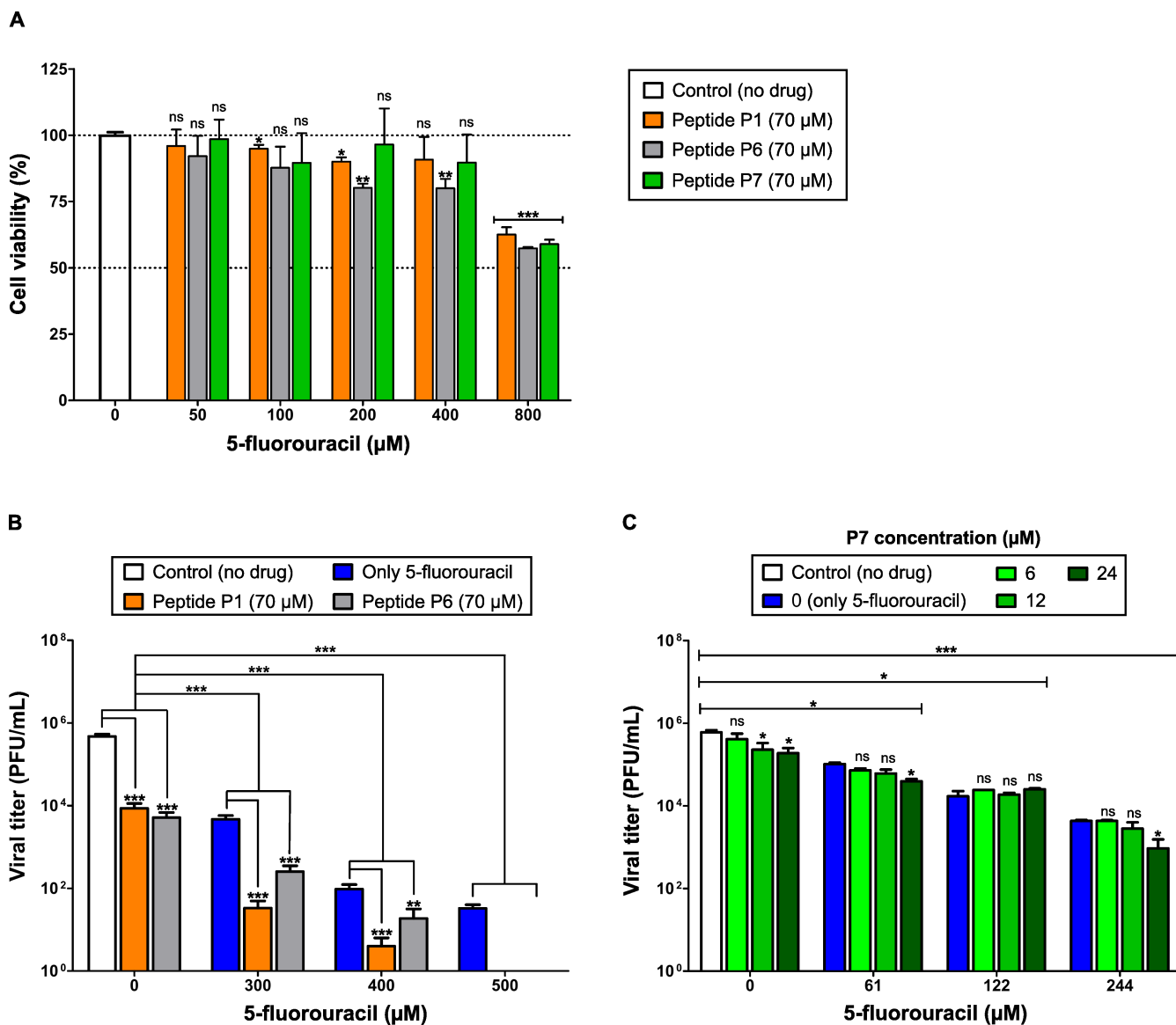


FIG 4 Screening and antiviral evaluation of peptide-5-fluorouracil combinations in Vero E6 cells. Cell viability (%) was measured by MTT assay after 72 h of exposure. Viral infectivity was quantified by plaque assay (PFU/mL) at 48 h post-infection. (A) Initial cytotoxicity screening of peptide-5-FU combinations. Vero E6 cells were treated with increasing concentrations of 5-FU in combination with peptides P1, P6, or P7 (70 µM). Cell viability data are summarized in Table S4A. (B) Antiviral activity of selected peptide-5-FU combinations. Cultures were treated with increasing concentrations of 5-FU in combination with peptides P1 or P6 (70 µM), and viral titers were determined by plaque assay. Viral titer values are summarized in Table S4B. (C) Exploratory low-dose antiviral evaluation of peptide P7 in combination with 5-FU. Cultures were treated with graded doses of 5-FU (61–244 µM) in combination with P7 (6–24 µM) to assess antiviral effects near the IC₅₀ range of both compounds. Viral titer values are summarized in Table S4B. Bars represent mean ± SD ($n = 3$). For infectivity panels, two statistical comparisons were performed: (i) within each 5-FU concentration group, samples without peptide vs. samples treated with peptide; and (ii) between 5-FU-treated groups and the untreated control (X -axis = 0). White bars represent untreated controls (no drug). Statistical significance: * $P < 0.05$; ** $P < 0.01$; *** $P < 0.001$; ns, not significant.

concentrations; however, adding P7 did not produce a significant additional inhibitory effect except at 24 µM peptide (Fig. 4C).

Chou-Talalay analysis revealed robust synergy for 5-FU + P1 across all concentrations, with CI values ranging from 0.471 to 0.932 ($CI < 1$ indicates synergy) (Fig. S6). In contrast, 5-FU + P6 showed an antagonistic effect at low doses (300 µM) but became synergistic at high 5-FU concentrations. Drug interaction analysis for 5-FU + P7 revealed a general trend toward antagonism, with weak synergy ($CI = 0.831$) only at the lowest concentrations tested (61 µM 5-FU and 6 µM P7).

Effect of antivirals on the mutant spectra

Based on the culture results, we selected 5-FU and peptides P1 and P6 for a more detailed characterization of their antiviral effects. These conditions were chosen to evaluate how treatments modulated SARS-CoV-2 mutant spectra from RNA extracted from treated cultures.

Specific infectivity of SARS-CoV-2

5-FU monotherapy reduced viral titer by 10^2 -fold to 10^4 -fold, while RNA load remained relatively stable, with at most a ~ 10 -fold reduction at 500 μM . As a result, SI decreased by ~ 100 -fold (10^{-4} – 10^{-6} PFU/RNA genomes, Fig. 5; Table S4C), indicating that 5-FU primarily impaired infectivity without substantially suppressing viral RNA replication.

In contrast, peptides P1 and P6 reduced both viral titer and RNA load (~ 100 -fold), leading to SI values similar to those of untreated controls (Fig. 5). This pattern suggests an inhibitory effect predominantly associated with viral replication.

Combined treatments produced complementary outcomes: peptides limited RNA genome accumulation, whereas 5-FU intensified loss of infectivity, particularly in combination with P1. As a consequence, SI values under combined treatments were markedly reduced and approached those observed for 5-FU monotherapy (Fig. 5; Table S4C). Overall, these results indicate that the combinations enhance infectivity inhibition while leaving RNA replication largely unaffected.

Mutation spectra and genetic diversity under drug exposure

The impact of antiviral treatments on both the number of mutations and the genetic diversity of mutant spectra was evaluated.

Consensus sequences were identical across all treatments (Fig. S2; Table S5A). Analysis of minority variation within the mutant spectra revealed that U \rightarrow C and A \rightarrow G transitions predominated under all conditions (Fig. 6; Table S5B and C). Most mutations appeared at very low frequencies (0.2%–1%), and only a small fraction exceeded 1% (Fig. S7).

5-FU treatment increased the number of mutations and the genetic diversity in a dose-dependent manner (Fig. 6 and 7; Table S5D), with statistically significant differences at 500 μM (Table S5E), confirming that high analog concentrations markedly alter the mutant spectra.

Peptides P1 and P6 alone did not significantly affect the number of mutations or diversity indices (Fig. 6 and 7; Table S5D). Their values remained significantly lower than those measured under all 5-FU treatments (Table S5E), indicating that the peptides do not exhibit mutagenic activity *per se*.

Combined treatments displayed a characteristic dose-dependent pattern. At low 5-FU concentrations (300 μM), the presence of peptides increased the number of mutations and diversity indices above those produced by the analog alone. As the 5-FU dose increased, the peptide co-treatment attenuated the diversity expansion normally induced by 5-FU. Thus, at 500 μM , the combinations generated significantly fewer mutations and lower diversity than 5-FU monotherapy, although still above untreated control levels (Fig. 6 and 7; Table S5D and E).

Distinct peptide-specific patterns were observed. In the 5-FU + P6 combination, mutation counts and diversity indices remained relatively stable across 5-FU doses. In contrast, the 5-FU + P1 combination showed a significant, dose-dependent decrease in genetic diversity (Fig. 6 and 7; Table S5D and E).

In addition, qualitative changes were observed in the distribution of mutations within the mutant spectra. The (A \rightarrow G+U \rightarrow C)/(G \rightarrow A+C \rightarrow U) ratio showed significant differences among treatments. As expected, 5-FU increased the frequency of U \rightarrow C mutations, but A \rightarrow G transitions remained similar to control groups. The analog also increased C \rightarrow U and G \rightarrow A transitions, thereby raising the Ts/Tv ratio (Tables S4C and 5D). Peptides P1 and P6 alone produced ratios comparable to the control. In contrast, the 5-FU + P1/6 combinations showed lower (A \rightarrow G+U \rightarrow C)/(G \rightarrow A+C \rightarrow U) and Ts/Tv ratios than 5-FU alone (Table

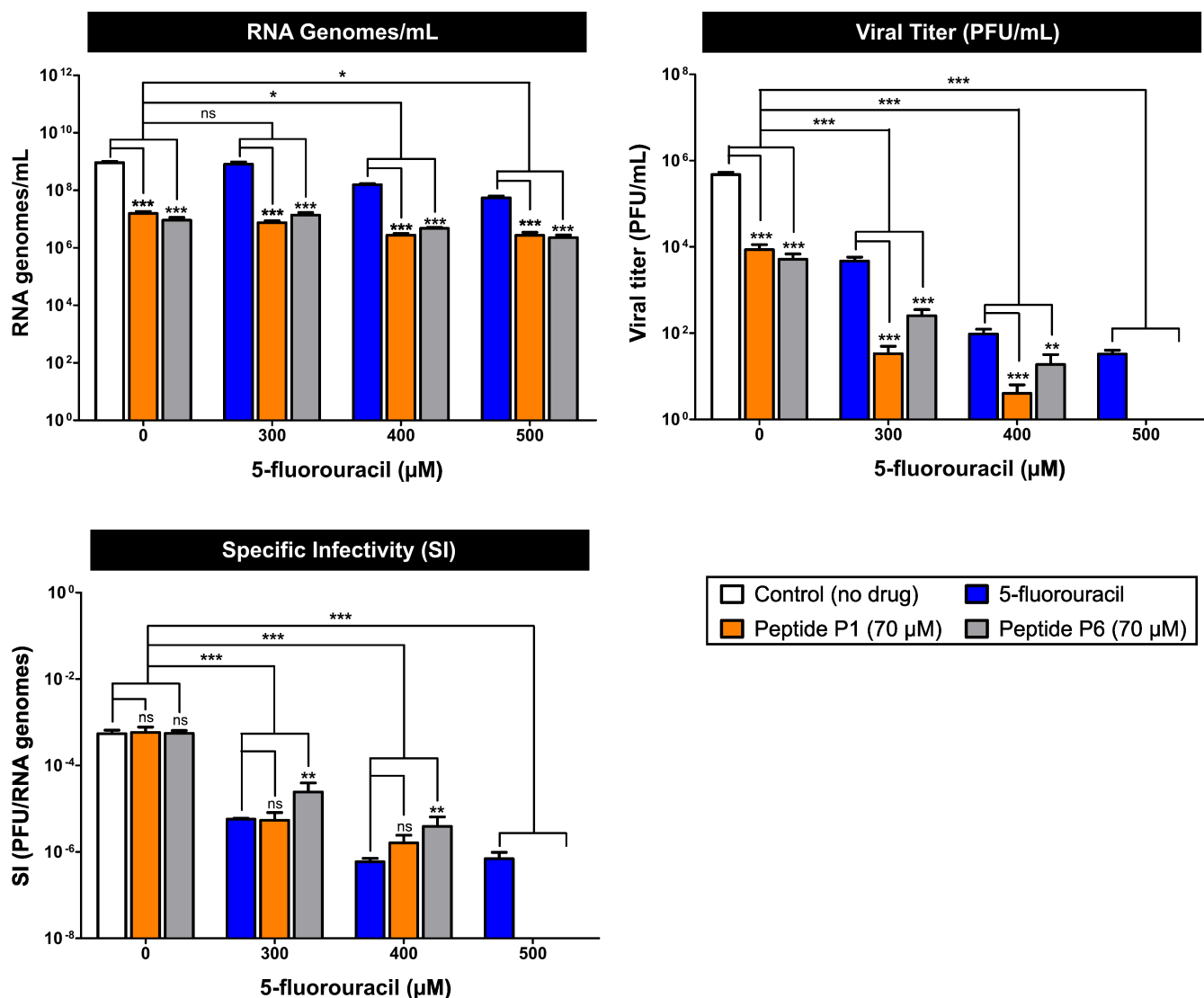


FIG 5 Effect of 5-FU and peptides P1 and P6 on the SI of SARS-CoV-2. Quantification of viral RNA copy number and viral infectivity (PFU/mL) under the indicated treatment conditions. Infectivity data, previously shown in Fig. 4, are presented here to provide an integrated overview of specific infectivity and mutant spectrum analyses. SI was calculated as the ratio of infectious units (PFU) to total viral RNA genomes. Bars represent mean \pm SD ($n = 3$). Two types of statistical analyses were performed: (i) within each 5-FU concentration group (0–500 μ M), comparing samples without peptide vs. samples treated with peptide; and (ii) between 5-FU-treated groups (300–500 μ M) and the untreated control (X-axis = 0). White bars represent untreated controls. Statistical significance: **P* < 0.05; ***P* < 0.01; ****P* < 0.001; ns, not significant. Complete infectivity, RNA, and SI data are summarized in Table S4C.

S5D), largely due to reduced accumulation of U→C transitions (Fig. 6) at higher analog concentrations, together with a relative increase in transversions (Table S5C). This pattern suggests that peptides may modulate how replication errors induced by 5-FU are processed, limiting the accumulation of dominant 5-FU-driven mutations. These compositional changes are consistent with the dinucleotide deviations detected under combination treatments (Fig. 6), supporting the notion that peptide co-treatments reshape the balance of transition and transversion events and thereby modulate the mutational signature normally imposed by 5-FU.

We next examined whether drug treatments altered the genomic distribution of mutations. Runs test analysis (Table S5F) showed that in untreated controls, mutations were distributed non-randomly across the genome ($P < 0.05$), driven mainly by ORF1ab, whereas other ORFs displayed random distributions. Except for the 300 μ M 5-FU condition, all treatments promoted a shift toward random distribution of mutations

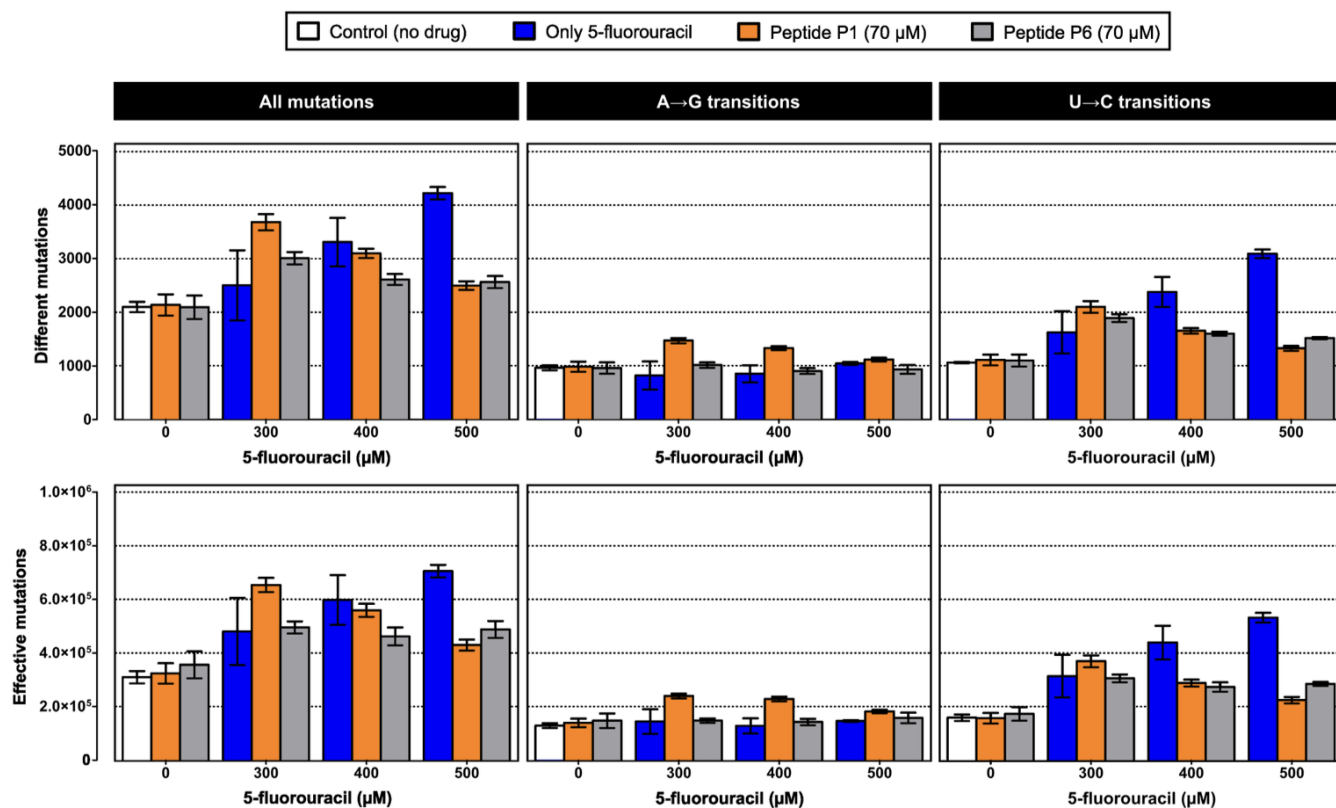


FIG 6 Mutation spectra of SARS-CoV-2 in the presence of 5-FU and peptides P1 and P6, alone or in combination. The plots show the number of different mutations (each counted once per sample) and the total number of effective mutations (each occurrence counted). The results are also shown separately for A→G and U→C transitions, which accounted for 75%–90% of all detected mutations. Bars are color-coded as in Fig. 4 and 5 (white, control; blue, 5-FU; orange, P1; gray, P6; mixed colors, combinations). Data represent mean \pm SD ($n = 3$). Statistical comparisons are summarized in Table S5E. Complete lists of mutations and their frequencies are provided in Table S5B through D.

within ORF1ab, suggesting that exposure to antiviral agents modifies how mutations are distributed across the viral genome.

Dinucleotide composition analysis supported these observations. Control samples displayed enriched G/C-rich dinucleotides, including CpG, and reduced A/U-rich dinucleotides such as UpA, consistent with the predominance of U→C and A→G transitions. 5-FU alone did not significantly alter dinucleotide O/E ratios. In contrast, both peptide-only and combination treatments produced detectable deviations (Fig. S8; Table S5G), including further reductions in A/U-rich dinucleotides and enhanced shifts associated with CpG-related pattern, in agreement with the diversity modulation observed in the mutant spectra.

Multivariate analysis of mutant spectra

To integrate the effects of 5-FU and peptide treatments on the overall population structure, we performed a principal component analysis (PCA) based on mutational composition. The first two components explained 83.18% of the total variance.

In the PCA plot (Fig. 8), untreated controls and peptide-only samples (P1 or P6) formed tight clusters, indicating highly homogeneous mutant spectra. Two of the three 300 μ M 5-FU replicates (SARS_FU300_B and SARS_FU300_C) also clustered with controls, whereas the third (SARS_FU300_A) was clearly displaced, indicating heterogeneous responses at intermediate analog doses.

Combination treatments showed greater dispersion and clear separation from controls. Three well-defined clusters emerged, corresponding to treatment type and 5-FU concentration. A dose-dependent trend was evident: higher 5-FU concentrations

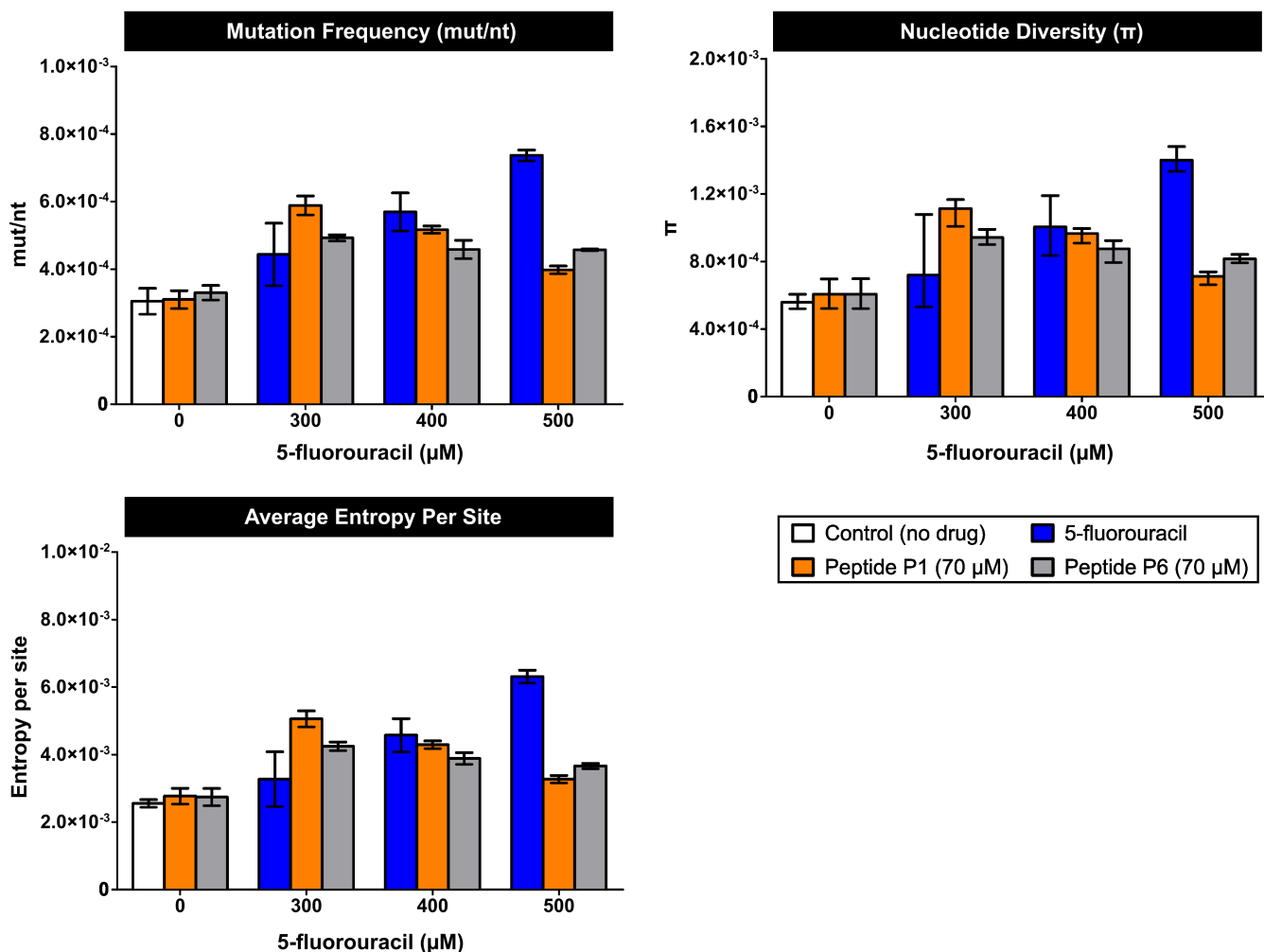


FIG 7 Genetic diversity of SARS-CoV-2 mutant spectra in the presence of 5-FU and peptides P1 and P6, alone or in combination. Diversity indices were calculated from NGS data and include mutation frequency, nucleotide diversity (π), and average Shannon entropy per site. Bars are color-coded as in Fig. 4 and 5 (white, control; blue, 5-FU; orange, P1; gray, P6; mixed colors combinations). Data represent mean \pm SD ($n = 3$). Statistical analyses are provided in Table S5E, and complete diversity values in Table S5D.

progressively shifted samples further from the control/peptide clusters, indicating increasing divergence in mutational profiles.

Interestingly, the 5-FU + P1 combinations exhibited a modulatory effect. At 500 μM 5-FU, replicates clustered closer to controls and peptide-only treatments, suggesting that P1 attenuated the broad diversification induced by high-dose 5-FU. At 300 μM , however, P1 + 5-FU formed a distinct cluster shifted along PC2, separate from both controls and 5-FU alone. Combinations with P6 followed a similar but less pronounced pattern.

Finally, the 500 μM 5-FU monotherapy replicates, along with the divergent SARS_FU300_A sample, formed a compact cluster at the positive end of PC1, demonstrating that high-dose 5-FU was the dominant driver of quasispecies diversification, whereas peptides introduced secondary, concentration-dependent modulations.

DISCUSSION

The decline in vaccine efficacy against emerging SARS-CoV-2 variants has underscored the need for complementary antiviral approaches capable of limiting viral replication and reducing immune escape. In this context, our study presents a dual antiviral

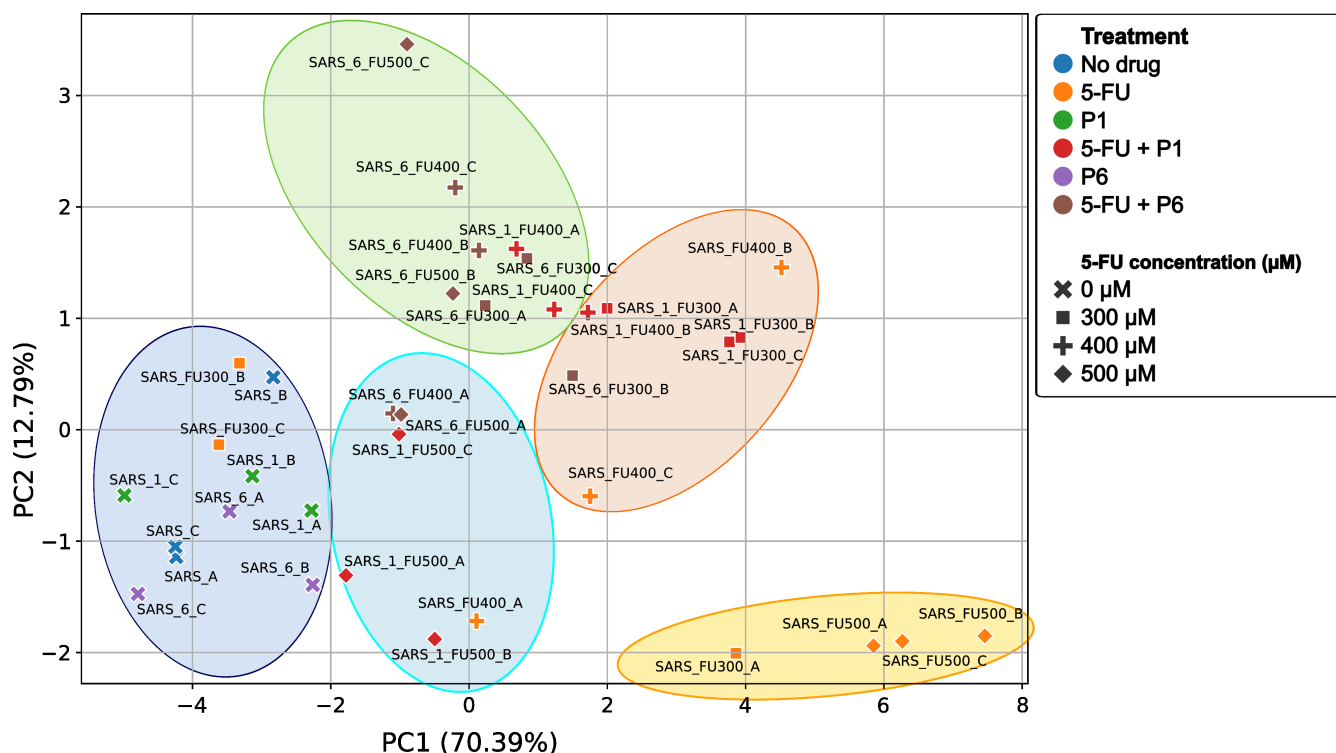


FIG 8 PCA of SARS-CoV-2 mutant spectra under different treatments. The scatter plot shows clustering of viral populations according to their mutational composition. The first two principal components explained 70.39% (PC1) and 12.79% (PC2) of the total variance. Controls (no drug, blue) and peptide-only treatments (P1, green; P6, magenta) formed tight clusters, whereas 5-FU monotherapy (orange) and combination treatments (5-FU + P1, red; 5-FU + P6, brown) showed distinct separation, depending on the analog concentration. Symbols indicate 5-FU doses: 0 μM (x), 300 μM (square), 400 μM (+), and 500 μM (diamond). Complete PCA parameters are provided in Table S5H, with additional visualizations in Fig. S9.

approach that combines SARS-CoV-2-derived inhibitory peptides designed to target replication complex functions with lethal mutagenesis.

The pyrimidine analog 5-FU, widely used in chemotherapy for its inhibition of DNA synthesis (64), has also been shown to induce lethal mutagenesis in multiple RNA viruses by increasing mutation frequency and promoting the accumulation of deleterious mutations (18, 20, 47, 62). The peptides designed in this study are derived from nsp10, an essential cofactor of the coronavirus replication complex that activates the nsp14 exonuclease (ExoN) and stimulates the nsp16 2'-O-methyltransferase (2'-O-MTase) (34, 40, 45, 65–67).

Our computational predictions indicated that mutations increasing guanine and cytosine content impose the highest fitness penalties on SARS-CoV-2. This may help explain the discrepancy between the dominant mutations observed in mutant spectra (U→C and A→G) (68, 69) and the substitutions that become fixed in viral populations, where C→U mutations predominate (70, 71). Based on genomic dinucleotide frequencies, we identified which dinucleotides favor SARS-CoV-2 replication and confirmed the particularly detrimental effect of CpG, consistent with strong host immune pressure reported previously (72, 73). This rationale supported the selection of 5-FU, as it preferentially generates U→C and A→G transitions (18, 20, 62, 74). However, the fitness cost of specific substitutions differs across proteins, likely reflecting variation in structural stability (75) and protein-protein interfaces, where deleterious effects can be amplified (76). In nsp10, U→G and U→A were the most detrimental substitutions. Mutations that change uracil to any other nucleotide are especially detrimental for viral fitness, as they have the effect of reducing the hydrophobicity of the protein (77), since U in the second position almost always codes for hydrophobic amino acids. On the other hand, in the nsp10-nsp14 and nsp10-nsp16 complexes, G→U and C→U had the strongest predicted

effects, consistent with their hydrophobic interfaces, where increased hydrophobicity can destabilize protein-protein interactions (78). These analyses highlight the limitations of prediction frameworks based solely on dinucleotide composition, as mutational impact also depends on the number, location, and structural consequences of substitution, at the nucleotide and protein levels, including effects on genomic features such as RNA secondary structures (79–81).

We did not test combinations of different peptides because several inhibitors were designed from the same nsp10 segment (residues 39–47: TNCVKMLCT), raising the possibility of competition for overlapping binding interfaces. Although each peptide was independently optimized for its target, interactions with shared nsp10 surfaces cannot be excluded (44, 54). Combining peptides could therefore hinder effective intracellular interactions by promoting competition, limiting antiviral potential (82–84). In addition, inhibition of the nsp10-nsp14 complex may affect not only ExoN but also N7-methyltransferase (N7-MTase) activity due to functional crosstalk between domains (44, 85) and could consequently impair mRNA capping and subsequent 2'-O-MTase function by nsp16.

The peptides exhibited markedly different IC₅₀ and CC₅₀ values despite high sequence similarity. For example, P1 and P2 differ by only two residues, yet displayed distinct cytotoxicity and antiviral activity. Even minor amino acid changes can strongly alter stability and interaction efficiency (86, 87). Native nsp10-derived peptide fragments were not evaluated experimentally, as the study focused on structure-guided optimized peptides with physicochemical properties compatible with cell-based antiviral assays. Peptide design required balancing hydrophobicity, necessary for membrane penetration and target binding (88), with solubility and low cytotoxicity (89, 90). Residues prone to chemical instability (e.g., Asp, which forms aspartimides) or redox reactivity (e.g., Cys) were avoided (91, 92). Cellular uptake also varied: P1 internalized more efficiently than P7, consistent with its higher positive charge, which promotes interactions with membrane proteoglycans and endocytic entry (93, 94). However, peptide uptake experiments were intended as a qualitative assessment of cellular association and fluorescence distribution. Surface-associated fluorescence cannot be fully excluded based on these images alone, and GFP alone was not included as a control in this assay. Importantly, peptide concentrations used in uptake experiments did not induce detectable cytotoxicity, arguing against major disruption of plasma membrane integrity. Although P7 showed antiviral activity, its evaluation was limited to internalization studies and low-dose combinations due to its narrower potency range relative to P1 and P6.

In our culture assays, 5-FU reduced SARS-CoV-2 titers by 100-fold to 10,000-fold at concentrations of 200–500 μ M, among the strongest inhibitory effects reported for coronaviruses. In contrast, SARS-CoV exhibited only modest reductions (3-fold to 10-fold) at comparable concentrations (34), suggesting greater susceptibility of SARS-CoV-2 to nucleoside analogs, consistent with observations for β -D-N⁴-hydroxycytidine (NHC) (95–97). Differences in proofreading efficiency (98, 99) and the slightly higher mutation rate of SARS-CoV-2 (100) compared with SARS-CoV (101) may contribute to this increased susceptibility.

The combination of 5-FU with peptides P1 or P6 produced a markedly synergistic antiviral effect, most evident in infectivity assays. Peptide monotherapy reduced both infectious titers and RNA levels, and the addition of 500 μ M 5-FU eliminated detectable infectivity, an outcome not achievable with 5-FU alone at non-cytotoxic concentrations. Synergistic effects typically emerge when drugs target complementary replication processes (102–105), as observed with combinations such as molnupiravir plus TMPRSS2 inhibitors (106) or ribavirin plus remdesivir, which achieved viral extinction in culture (23). Such combinations improve efficacy and reduce toxicity by lowering required doses (107–109). When ribavirin is combined with remdesivir (23) or nirmatrelvir (110), lower concentrations of each drug are needed to inhibit SARS-CoV-2 replication.

Analysis of mutant spectra confirmed that 5-FU primarily reduced infectivity without strongly affecting genome replication, a hallmark of lethal defection (18, 111–113).

Peptides alone exhibited only weak mutagenic activity, which may be consistent with partial interference with nsp14-dependent proofreading (34, 66, 114). Their modest effects on diversity may reflect limitations in intracellular stability and access. Unlike nucleoside analogs, peptides face barriers including protease degradation, low membrane permeability, rapid clearance, and potential immunogenicity (115–117). Additionally, SARS-CoV-2's high mutation rate could generate variants with altered peptide sensitivity, even without direct mutations at binding sites (118, 119). Interference with nsp16 methyltransferase activity may also contribute to antiviral effects, as disruption of 5'-cap formation can impair viral RNA synthesis (120–122). Indeed, peptide treatments caused a substantial reduction in viral RNA relative to controls and 5-FU alone, suggesting that decreased replication could counterbalance mutational accumulation.

Patterns of genetic diversity under combination treatments provided additional insight into viral evolutionary responses to drug pressure. Dual treatment reduced genetic diversity in mutant spectra relative to 5-FU alone, especially at 500 μ M, possibly due to peptide-induced suppression of replication rounds. Viral replication rate influences analog incorporation and reduced replication can limit mutagenesis (123–127). A reduction in replication may favor extinction, as replicative fitness itself can act as a resistance mechanism (128–130). However, not all analog combinations produce this effect, for example, ribavirin + remdesivir (23) and molnupiravir + nirmatrelvir (131).

The relationship between replication rate and analog-induced mutagenesis does not fully explain the qualitative changes in mutational spectra. If lower diversity were solely due to reduced replication rounds, all transitions would decrease proportionally. Instead, combination treatments produced decreases in the (A→G+U→C)/(G→A+C→U) ratio and Ts/Tv values, driven by a preferential reduction of U→C-5-FU's signature mutation, without comparable decreases in other transitions. This suggests that peptides P1 and P6 may interfere with 5-FU's mutagenic activity.

An intriguing dose-response pattern emerged at 300 μ M 5-FU; combination treatments increased genetic diversity relative to 5-FU alone, despite viral load decreasing ~100-fold. This indicates that reduced replication rounds did not limit 5-FU-induced mutagenesis at this dose and may reflect a phase of lethal defection, where specific infectivity falls while mutation counts rise (18, 111). However, at higher 5-FU concentrations, diversity decreased under dual treatment relative to monotherapy, particularly with P1, although viral load remained stable. These findings suggest that peptides modulate the mutagenic response to 5-FU, enhancing mutagenesis at moderate doses but dampening it at high doses. Whether this behavior reflects changes in 5-FU incorporation efficiency (as FUTP) (21, 132, 133) or differences in 5-FU metabolism remains unknown and warrants further study through quantification of 5-FU metabolites and targeted proteomics.

Peptide-mediated interference with nsp14- and nsp16-associated functions may also affect post-replicative RNA maturation and innate immune evasion. These enzymes are essential for 5'-cap formation, which masks viral RNA from host sensors (134, 135). A previous study showed that an nsp16-targeting peptide (TP29) enhanced IFN-I production in mouse cells (46). This mechanism could not be evaluated in Vero E6 cells due to their lack of IFN- α/β genes (136). Although these cells can retain partial responses via IFN- λ downstream signaling pathways (RLR, Jak-STAT, TLR, and MAPK), immunomodulatory effects of peptide inhibition are likely underestimated (137, 138). Furthermore, differences in cytopathic effects between Vero E6 and human cells, particularly for Omicron variants, highlight the need for testing in immune-competent, physiologically relevant models (139). Therefore, confirmation of these antiviral effects in additional human respiratory cell systems will be an important objective for future studies. Moreover, changes in dinucleotide composition observed under peptide + 5 FU treatments reinforce this interpretation. CpG and UpA suppression are deeply conserved features of coronavirus genomes linked to innate immune evasion and RNA stability (30–32, 140), and even moderate deviations from these patterns can indicate perturbations

of population robustness and genome architecture. The shifts detected in our combined treatment, therefore, suggest that dual therapy not only alters mutation frequency and diversity but also modulates structural constraints on genome composition, potentially reshaping the mutational landscape that sustains SARS-CoV-2 quasispecies dynamics. Such compositional deviations further support the view that quasispecies dynamics, rather than isolated mutations, underline the response of SARS-CoV-2 populations to combined mutagenic and peptide-based inhibition.

Although direct peptide-protein binding was not experimentally assessed in this study, the structure-guided design, conservation of the targeted interfaces, and the observed antiviral and synergistic effects are consistent with functional interference at nsp10-associated replication complexes, although additional biochemical studies will be required to fully define the underlying molecular interactions.

In conclusion, combining 5-fluorouracil with nsp10-derived peptides predicted to interfere with nsp14- and nsp16-associated functions produces a potent synergistic antiviral effect, markedly reducing SARS-CoV-2 infectivity. This dual mechanism, acting on proofreading- and methylation-associated processes while enhancing mutagenesis, supports the promise of peptide-nucleoside analog combinations as a broad-spectrum antiviral strategy. However, the behavior of mutant spectra under dual treatment remains complex and requires additional studies to clarify underlying mechanisms. Future work in immune-competent systems and across diverse viral variants will be crucial to validate the efficacy, safety, and translational potential of this approach as a potential pan-coronavirus therapeutic platform.

ACKNOWLEDGMENTS

This work was funded by grant CV20-10932 (PI: AG-P) from the Junta de Andalucía, co-financed with FEDER funds, and partially funded by Fundación Bancaria Unicaja. Partial funding for open access charges was provided by the Universidad de Málaga. U.B. was supported by grant PID2023-151032NB-C2 from the Spanish Ministry of Science (MCIU), the Spanish Research Agency (AEI/10.13039/501100011033/), and FEDER, EU. Research at the CBMSO is facilitated by the Fundación Ramón Areces and supported by the Ministerio de Ciencia, Innovación y Universidades (MICIU), through grant PID2023-146622OB-I00, financed by MICIU/AEI/10.13039/501100011033 and FEDER, EU, and by the “Severo Ochoa” Program for Centres of Excellence in Research and Development (CEX2021- 001154-S). We also acknowledge project TEC-607 2024/BIO-66 (SALAINDEC-CM from Comunidad de Madrid/FEDER).

S.O.D.C. acknowledges financial support from Fundación Martín Varona. A.M.F.E. acknowledges a Teaching Staff Retraining Grant (2023), Spanish Ministry of Universities, and CIBEST/2024/114 from Generalitat Valenciana. We thank Dr. Luis Enjuanes (CNB-CSIC, Spain) for providing Vero E6 cells and Dr. Francisco Sobrino (CBMSO) for providing the VFA control peptide.

AUTHOR AFFILIATIONS

¹Área de Genética, Facultad de Ciencias, Campus de Teatinos, Universidad de Málaga, Málaga, Spain

²Instituto de Investigación en Biotecnología y Salud (IDiBE), Universidad Miguel Hernández, Elche, Spain

³Department of Public Health, History of Science and Gynecology, Universidad Miguel Hernández, Sant Joan d'Alacant, Spain

⁴Centro de Supercomputación y Bioinnovación (SCBI), Universidad de Málaga, Málaga, Spain

⁵Centro de Biología Molecular Severo Ochoa (CBM), (Consejo Superior de Investigaciones Científicas-Universidad Autónoma de Madrid) (CSIC-UAM), Campus de Cantoblanco, Madrid, Spain

⁶Department of Clinical Microbiology, Instituto de Investigación Sanitaria-Fundación Jiménez Díaz University Hospital, Universidad Autónoma de Madrid (IIS-FJD, UAM), Madrid, Spain

⁷Servicios Centrales de Apoyo a la Investigación (SCAI), Área de Ciencias de la Vida, Genómica, Universidad de Málaga, Málaga, Spain

⁸Hospital Universitario Virgen de la Victoria, Campus de Teatinos, Málaga, Spain

⁹Instituto de Investigación Biomédica de Málaga y Plataforma en Nanomedicina (IBIMA Plataforma-BIONAND), Universidad de Málaga, Málaga, Spain

PRESENT ADDRESS

Francisco José Villena González, Bioinformatics Unit, Centro Nacional de Investigaciones Oncológicas (CNIO), Madrid, Spain

AUTHOR ORCIDs

Sergio Ortega Del Campo <http://orcid.org/0000-0002-3975-6951>

Gregorio Joaquín Fernández Ballester <http://orcid.org/0000-0002-5412-8611>

Clara Blanes Mira <http://orcid.org/0000-0002-9625-6275>

Luis Díaz Martínez <http://orcid.org/0000-0002-7659-4349>

Ana Isabel de Ávila <http://orcid.org/0000-0002-9381-0963>

María Eugenia Soria <http://orcid.org/0000-0002-4719-3351>

Brenda Martínez-González <http://orcid.org/0000-0002-4482-5181>

Francisco José Villena González <http://orcid.org/0009-0006-9119-1093>

Josefa Gómez-Maldonado <http://orcid.org/0000-0003-1570-1937>

Encarnación Clavijo Frutos <http://orcid.org/0000-0002-0172-5164>

Ugo Bastolla <http://orcid.org/0000-0001-9342-4678>

Celia Perales <http://orcid.org/0000-0003-1618-1937>

Esteban Domingo <http://orcid.org/0000-0002-0573-1676>

Enrique Viguera <http://orcid.org/0000-0001-5475-3807>

Ana María Fernández Escamilla <http://orcid.org/0000-0002-6615-4913>

Ana Grande Pérez <http://orcid.org/0000-0002-2821-062X>

FUNDING

Funder	Grant(s)	Author(s)
Fundación Ramón Areces	Research funding	Celia Perales Esteban Domingo
Universidad de Málaga	Open access	Enrique Viguera Ana Grande Pérez
Ministerio de Ciencia, Innovación y Universidades	PID2023-151032NB-C2	Ugo Bastolla
Generalitat Valenciana	CIBEST/2024/114	Ana María Fernández Escamilla
Junta de Andalucía	CV20-10932	Ana Grande Pérez
Ministerio de Universidades (MU)	Teaching Staff Retraining Grant (2023)	Ana María Fernández Escamilla
Spanish Agency of Research and FEDER	AEI/10.13039/501100011033/	Ugo Bastolla
Fundacion Martin Varona	Financial support	Sergio Ortega Del Campo
Fundacion Bancaria Unicaja		Ana Grande Pérez

Funder	Grant(s)	Author(s)
Ministerio de Ciencia, Innovación y Universidades, "Severo Ochoa" Program for Centres of Excellence in Research and Development	PID2023-146622OB-I00, CEX2021-001154-S	Celia Perales
SALAINDEC-CM, Comunidad de Madrid/FEDER	TEC-607 2024/BIO-66	Celia Perales

DATA AVAILABILITY

The data generated and analyzed in the present study are included in this manuscript and the supplementary material. Additional information is available from the corresponding author upon reasonable request.

Illumina raw read data has been uploaded to the Sequence Read Archive (SRA) database under accession ID [PRJNA1379670](https://www.ncbi.nlm.nih.gov/sra/PRJNA1379670).

ADDITIONAL FILES

The following material is available [online](#).

Supplemental Material

Supplemental figures (AAC01885-25-s0001.docx). Fig. S1 to S9.

Table S1 (AAC01885-25-s0002.xlsx). Materials and methods.

Table S2 (AAC01885-25-s0003.xlsx). Estimated effects of individual mutations on SARS-CoV-2 fitness.

Table S3 (AAC01885-25-s0004.xlsx). Evolutionary analysis of coronavirus proteins.

Table S4 (AAC01885-25-s0005.xlsx). Cell culture assays.

Table S5 (AAC01885-25-s0006.xlsx). Quasispecies analysis.

REFERENCES

- Farinholt T, Doddapaneni H, Qin X, Menon V, Meng Q, Metcalf G, Chao H, Gingras M-C, Farinholt P, Agrawal C, Muzny DM, Piedra PA, Gibbs RA, Petrosino J. 2021. Transmission event of SARS-CoV-2 Delta variant reveals multiple vaccine breakthrough infections. *medRxiv*:2021.06.28.21258780. <https://doi.org/10.1101/2021.06.28.21258780>
- García-Beltrán WF, Lam EC, St Denis K, Nitido AD, García ZH, Hauser BM, Feldman J, Pavlovic MN, Gregory DJ, Poznansky MC, Sigal A, Schmidt AG, Iafate AJ, Naranbhai V, Balazs AB. 2021. Multiple SARS-CoV-2 variants escape neutralization by vaccine-induced humoral immunity. *Cell* 184:2372–2383. <https://doi.org/10.1016/j.cell.2021.03.013>
- Hoffmann M, Krüger N, Schulz S, Cossmann A, Rocha C, Kempf A, Nehlmeier I, Graichen L, Moldenhauer A-S, Winkler MS, Lier M, Dopfer-Jablonka A, Jäck H-M, Behrens GMN, Pöhlmann S. 2022. The Omicron variant is highly resistant against antibody-mediated neutralization: implications for control of the COVID-19 pandemic. *Cell* 185:447–456. <https://doi.org/10.1016/j.cell.2021.12.032>
- Kaku Y, Uriu K, Kosugi Y, Okumura K, Yamasoba D, Uwamino Y, Kuramochi J, Sadamasu K, Yoshimura K, Asakura H, Nagashima M, Ito J, Sato K, Genotype to Phenotype Japan (G2P-Japan) Consortium. 2024. Virological characteristics of the SARS-CoV-2 KP.2 variant. *Lancet Infect Dis* 24:e416. [https://doi.org/10.1016/S1473-3099\(24\)00298-6](https://doi.org/10.1016/S1473-3099(24)00298-6)
- Lewnard JA, Mahale P, Malden D, Hong V, Ackerson BK, Lewin BJ, Link-Gelles R, Feldstein LR, Lipsitch M, Tartof SY. 2024. Immune escape and attenuated severity associated with the SARS-CoV-2 BA.2.86/JN.1 lineage. *Nat Commun* 15:8550. <https://doi.org/10.1038/s41467-024-52668-w>
- Ma KC, Surie D, Lauring AS, Martin ET, Leis AM, Papalambros L, Gaglani M, Columbus C, Gottlieb RL, Ghamande S, et al. 2026. Effectiveness of updated 2023–2024 (Monovalent XBB.1.5) COVID-19 vaccination against SARS-CoV-2 Omicron XBB and BA.2.86/JN.1 lineage hospitalization and a comparison of clinical severity—IVY network, 26 hospitals, 18 October 2023–9 March 2024. *Clin Infect Dis* 82:e595–e603. <https://doi.org/10.1093/cid/ciae405>
- Domingo E, Sheldon J, Perales C. 2012. Viral quasispecies evolution. *Microbiol Mol Biol Rev* 76:159–216. <https://doi.org/10.1128/MMBR.05023-11>
- Domingo E, Perales C. 2019. Viral quasispecies. *PLoS Genet* 15:e1008271. <https://doi.org/10.1371/journal.pgen.1008271>
- Domingo E, Martín V, Perales C, Grande-Pérez A, García-Arriaza J, Arias A. 2006. Viruses as quasispecies: biological implications, p 51–82. *In* Domingo E (ed), *Quasispecies: concept and implications for virology*. Springer, Berlin Heidelberg, Berlin, Heidelberg.
- Moreno E, Gallego I, Gregori J, Lucía-Sanz A, Soria ME, Castro V, Beach NM, Manrubia S, Quer J, Esteban JI, Rice CM, Gómez J, Gastaminza P, Domingo E, Perales C. 2017. Internal disequilibria and phenotypic diversification during replication of hepatitis C virus in a noncoevolving cellular environment. *J Virol* 91:e02505-16. <https://doi.org/10.1128/JVI.02505-16>
- Donohue RC, Pfaller CK, Cattaneo R. 2019. Cyclical adaptation of measles virus quasispecies to epithelial and lymphocytic cells: to V, or not to V. *PLoS Pathog* 15:e1007605. <https://doi.org/10.1371/journal.ppat.1007605>
- Martínez-González B, Vázquez-Sirvent L, Soria ME, Mínguez P, Salar-Vidal L, García-Crespo C, Gallego I, de Ávila AI, Llorens C, Soriano B, Ramos-Ruiz R, Esteban J, Fernandez-Roblas R, Gadea I, Ayuso C, Ruíz-Hornillos J, Pérez-Jorge C, Domingo E, Perales C. 2022. Vaccine breakthrough infections with SARS-CoV-2 Alpha mirror mutations in Delta Plus, Iota, and Omicron. *J Clin Invest* 132:e157700. <https://doi.org/10.1172/JCI157700>
- Obasa AE, Ambikan AT, Gupta S, Neogi U, Jacobs GB. 2021. Increased acquired protease inhibitor drug resistance mutations in minor HIV-1 quasispecies from infected patients suspected of failing on national second-line therapy in South Africa. *BMC Infect Dis* 21:214. <https://doi.org/10.1186/s12879-021-05905-2>
- Ulzurrun E, Grande-Pérez A, Del Hoyo D, Guevara C, Gil C, Sorzano CO, Campillo NE. 2024. Unlocking the puzzle: non-defining mutations in

- SARS-CoV-2 proteome may affect vaccine effectiveness. *Front Public Health* 12:1386596. <https://doi.org/10.3389/fpubh.2024.1386596>
15. Moreno H, Grande-Pérez A, Domingo E, Martín V. 2012. Arenaviruses and lethal mutagenesis. Prospects for new ribavirin-based interventions. *Viruses* 4:2786–2805. <https://doi.org/10.3390/v4112786>
 16. Perales C, Gallego I, de Ávila AI, Soria ME, Gregori J, Quer J, Domingo E. 2019. The increasing impact of lethal mutagenesis of viruses. *Future Med Chem* 11:1645–1657. <https://doi.org/10.4155/fmc-2018-0457>
 17. Agudo R, de la Higuera I, Arias A, Grande-Pérez A, Domingo E. 2016. Involvement of a joker mutation in a polymerase-independent lethal mutagenesis escape mechanism. *Virology (Auckl)* 494:257–266. <https://doi.org/10.1016/j.virol.2016.04.023>
 18. Díaz-Martínez L, Brichette-Mieg I, Pineño-Ramos A, Domínguez-Huerta G, Grande-Pérez A. 2018. Lethal mutagenesis of an RNA plant virus via lethal defection. *Sci Rep* 8:1444. <https://doi.org/10.1038/s41598-018-19829-6>
 19. Graci JD, Gnädig NF, Galarraga JE, Castro C, Vignuzzi M, Cameron CE. 2012. Mutational robustness of an RNA virus influences sensitivity to lethal mutagenesis. *J Virol* 86:2869–2873. <https://doi.org/10.1128/JVI.05712-11>
 20. Grande-Pérez A, Gómez-Mariano G, Lowenstein PR, Domingo E. 2005. Mutagenesis-induced, large fitness variations with an invariant arenavirus consensus nucleotide sequence. *J Virol* 79:10451–10459. <https://doi.org/10.1128/JVI.79.16.10451-10459.2005>
 21. Gordon CJ, Tchesnokov EP, Schinazi RF, Götte M. 2021. Molnupiravir promotes SARS-CoV-2 mutagenesis via the RNA template. *J Biol Chem* 297:100770. <https://doi.org/10.1016/j.jbc.2021.100770>
 22. Kabinger F, Stiller C, Schmitzová J, Dienemann C, Kokic G, Hillen HS, Höbartner C, Cramer P. 2021. Mechanism of molnupiravir-induced SARS-CoV-2 mutagenesis. *Nat Struct Mol Biol* 28:740–746. <https://doi.org/10.1038/s41594-021-00651-0>
 23. García-Crespo C, de Ávila AI, Gallego I, Soria ME, Durán-Pastor A, Somovilla P, Martínez-González B, Muñoz-Flores J, Mínguez P, Salar-Vidal L, Esteban-Muñoz M, Cañar-Camacho E, Ferrer-Orta C, Zuñiga S, Sola I, Enjuanes L, Esteban J, Fernández-Roblas R, Gadea I, Gómez J, Verdaguier N, Domingo E, Perales C. 2024. Synergism between remdesivir and ribavirin leads to SARS-CoV-2 extinction in cell culture. *Br J Pharmacol* 181:2636–2654. <https://doi.org/10.1111/bph.16344>
 24. Odon V, Fiddaman SR, Smith AL, Simmonds P. 2022. Comparison of CpG- and UpA-mediated restriction of RNA virus replication in mammalian and avian cells and investigation of potential ZAP-mediated shaping of host transcriptome compositions. *RNA* 28:1089–1109. <https://doi.org/10.1261/rna.079102.122>
 25. Simmonds P, Xia W, Baillie JK, McKinnon K. 2013. Modelling mutational and selection pressures on dinucleotides in eukaryotic phyla –selection against CpG and UpA in cytoplasmically expressed RNA and in RNA viruses. *BMC Genomics* 14:610. <https://doi.org/10.1186/1471-2164-14-610>
 26. Ficarelli M, Wilson H, Pedro Galão R, Mazzon M, Antzin-Andueta I, Marsh M, Neil SJ, Swanson CM. 2019. KHNYN is essential for the zinc finger antiviral protein (ZAP) to restrict HIV-1 containing clustered CpG dinucleotides. *eLife* 8:e46767. <https://doi.org/10.7554/eLife.46767>
 27. Ly PT, Xu S, Wirawan M, Luo D, Roca X. 2022. ZAP isoforms regulate unfolded protein response and epithelial-mesenchymal transition. *Proc Natl Acad Sci USA* 119:e2121453119. <https://doi.org/10.1073/pnas.2121453119>
 28. Nchioua R, Kmiec D, Müller JA, Conzelmann C, Groß R, Swanson CM, Neil SJD, Stenger S, Sauter D, Münch J, Sparrer KJM, Kirchhoff F. 2020. SARS-CoV-2 is restricted by zinc finger antiviral protein despite preadaptation to the low-CpG environment in humans. *mBio* 11:e01930-20. <https://doi.org/10.1128/mBio.01930-20>
 29. Afrasiabi A, Alinejad-Rokny H, Khosh A, Rahnama M, Lovell N, Xu Z, Ebrahimi D. 2022. The low abundance of CpG in the SARS-CoV-2 genome is not an evolutionarily signature of ZAP. *Sci Rep* 12:2420. <https://doi.org/10.1038/s41598-022-06046-5>
 30. Oliver JL, Bernaola-Galván P, Carpena P, Perfectti F, Gómez-Martín C, Castiglione S, Raia P, Verdú M, Moya A. 2025. Strong evidence for the evolution of decreasing compositional heterogeneity in SARS-CoV-2 genomes during the pandemic. *Sci Rep* 15:12246. <https://doi.org/10.1038/s41598-025-95893-z>
 31. Simmonds P. 2024. C→U transition biases in SARS-CoV-2: still rampant 4 years from the start of the COVID-19 pandemic. *mBio* 15:e0249324. <https://doi.org/10.1128/mbio.02493-24>
 32. Xia X. 2020. Extreme genomic CpG deficiency in SARS-CoV-2 and evasion of host antiviral defense. *Mol Biol Evol* 37:2699–2705. <https://doi.org/10.1093/molbev/msaa094>
 33. Peck KM, Lauring AS. 2018. Complexities of viral mutation rates. *J Virol* 92:e01031-17. <https://doi.org/10.1128/JVI.01031-17>
 34. Smith EC, Blanc H, Vignuzzi M, Denison MR. 2013. Coronaviruses lacking exoribonuclease activity are susceptible to lethal mutagenesis: evidence for proofreading and potential therapeutics. *PLoS Pathog* 9:e1003565. <https://doi.org/10.1371/journal.ppat.1003565>
 35. Heydari H, Golmohammadi R, Mirnejad R, Tebyanian H, Fasihi-Ramandi M, Moosazadeh Moghaddam M. 2021. Antiviral peptides against *Coronaviridae* family: a review. *Peptides* 139:170526. <https://doi.org/10.1016/j.peptides.2021.170526>
 36. Struck A-W, Axmann M, Pfefferle S, Drosten C, Meyer B. 2012. A hexapeptide of the receptor-binding domain of SARS corona virus spike protein blocks viral entry into host cells via the human receptor ACE2. *Antiviral Res* 94:288–296. <https://doi.org/10.1016/j.antiviral.2011.12.012>
 37. Xia S, Liu M, Wang C, Xu W, Lan Q, Feng S, Qi F, Bao L, Du L, Liu S, Qin C, Sun F, Shi Z, Zhu Y, Jiang S, Lu L. 2020. Inhibition of SARS-CoV-2 (previously 2019-nCoV) infection by a highly potent pan-coronavirus fusion inhibitor targeting its spike protein that harbors a high capacity to mediate membrane fusion. *Cell Res* 30:343–355. <https://doi.org/10.1038/s41422-020-0305-x>
 38. Baddock HT, Brolih S, Yosaatmadja Y, Ratnaweera M, Bielinski M, Swift LP, Cruz-Migoni A, Fan H, Keown JR, Walker AP, Morris GM, Grimes JM, Fodor E, Schofield CJ, Gileadi O, McHugh PJ. 2022. Characterization of the SARS-CoV-2 ExoN (nsp14^{ExoN}-nsp10) complex: implications for its role in viral genome stability and inhibitor identification. *Nucleic Acids Res* 50:1484–1500. <https://doi.org/10.1093/nar/gkab1303>
 39. Romano M, Ruggiero A, Squeglia F, Maga G, Berisio R. 2020. A structural view of SARS-CoV-2 RNA replication machinery: RNA synthesis, proofreading and final capping. *Cells* 9:1267. <https://doi.org/10.3390/ce11s9051267>
 40. Bouvet M, Lugari A, Posthuma CC, Zevenhoven JC, Bernard S, Betzi S, Imbert I, Canard B, Guillemot J-C, Lécine P, Pfefferle S, Drosten C, Nijder EJ, Decroly E, Morelli X. 2014. Coronavirus Nsp10, a critical co-factor for activation of multiple replicative enzymes. *J Biol Chem* 289:25783–25796. <https://doi.org/10.1074/jbc.M114.577353>
 41. Wang H, Rizvi SRA, Dong D, Lou J, Wang Q, Sopipong W, Su Y, Najaf F, Agarwal PK, Kozielski F, Haider S. 2023. Emerging variants of SARS-CoV-2 NSP10 highlight strong functional conservation of its binding to two non-structural proteins, NSP14 and NSP16. *eLife* 12:RP87884. <https://doi.org/10.7554/eLife.87884>
 42. Arabi-Jeshvaghani F, Javadi-Zarnaghi F, Ganjalikhany MR. 2023. Analysis of critical protein-protein interactions of SARS-CoV-2 capping and proofreading molecular machineries towards designing dual target inhibitory peptides. *Sci Rep* 13:350. <https://doi.org/10.1038/s41598-022-26778-8>
 43. Ke M, Chen Y, Wu A, Sun Y, Su C, Wu H, Jin X, Tao J, Wang Y, Ma X, Pan J-A, Guo D. 2012. Short peptides derived from the interaction domain of SARS coronavirus nonstructural protein nsp10 can suppress the 2'-O-methyltransferase activity of nsp10/nsp16 complex. *Virus Res* 167:322–328. <https://doi.org/10.1016/j.virusres.2012.05.017>
 44. Kozielski F, Sele C, Talibov VO, Lou J, Dong D, Wang Q, Shi X, Nyblom M, Rogstam A, Krojer T, Fisher Z, Knecht W. 2022. Identification of fragments binding to SARS-CoV-2 nsp10 reveals ligand-binding sites in conserved interfaces between nsp10 and nsp14/nsp16. *RSC Chem Biol* 3:44–55. <https://doi.org/10.1039/d1cb00135c>
 45. Smith EC, Case JB, Blanc H, Isakov O, Shomron N, Vignuzzi M, Denison MR. 2015. Mutations in coronavirus nonstructural protein 10 decrease virus replication fidelity. *J Virol* 89:6418–6426. <https://doi.org/10.1128/JVI.00110-15>
 46. Wang Y, Sun Y, Wu A, Xu S, Pan R, Zeng C, Jin X, Ge X, Shi Z, Ahola T, Chen Y, Guo D. 2015. Coronavirus nsp10/nsp16 methyltransferase can be targeted by nsp10-derived peptide *in vitro* and *in vivo* to reduce replication and pathogenesis. *J Virol* 89:8416–8427. <https://doi.org/10.1128/JVI.00948-15>
 47. Bassi MR, Sempere RN, Meyn P, Polacek C, Arias A. 2018. Extinction of Zika virus and Usutu virus by lethal mutagenesis reveals different patterns of sensitivity to three mutagenic drugs. *Antimicrob Agents Chemother* 62:e00380. <https://doi.org/10.1128/AAC.00380-18>

48. Bastolla U. 2014. Detecting selection on protein stability through statistical mechanical models of folding and evolution. *Biomolecules* 4:291–314. <https://doi.org/10.3390/biom4010291>
49. Bastolla U, Vendruscolo M, Knapp E-W. 2000. A statistical mechanical method to optimize energy functions for protein folding. *Proc Natl Acad Sci USA* 97:3977–3981. <https://doi.org/10.1073/pnas.97.8.3977>
50. Minning J, Porto M, Bastolla U. 2013. Detecting selection for negative design in proteins through an improved model of the misfolded state. *Proteins* 81:1102–1112. <https://doi.org/10.1002/prot.24244>
51. Derrida B. 1981. Random-energy model: an exactly solvable model of disordered systems. *Phys Rev B* 24:2613–2626. <https://doi.org/10.1103/PhysRevB.24.2613>
52. de la Higuera I, Ferrer-Orta C, de Ávila AI, Perales C, Sierra M, Singh K, Sarafianos SG, Dehouck Y, Bastolla U, Verdaguer N, Domingo E. 2017. Molecular and functional bases of selection against a mutation bias in an RNA virus. *Genome Biol Evol* 9:1212–1228. <https://doi.org/10.1093/gbe/evx075>
53. Katoh K, Rozewicki J, Yamada KD. 2019. MAFFT online service: multiple sequence alignment, interactive sequence choice and visualization. *Brief Bioinform* 20:1160–1166. <https://doi.org/10.1093/bib/bbx108>
54. Lin S, Chen H, Chen Z, Yang F, Ye F, Zheng Y, Yang J, Lin X, Sun H, Wang L, Wen A, Dong H, Xiao Q, Deng D, Cao Y, Lu G. 2021. Crystal structure of SARS-CoV-2 nsp10 bound to nsp14-ExoN domain reveals an exoribonuclease with both structural and functional integrity. *Nucleic Acids Res* 49:5382–5392. <https://doi.org/10.1093/nar/gkab320>
55. Rosas-Lemus M, Minasov G, Shuvalova L, Inniss NL, Kiryukhina O, Brunzelle J, Satchell KJF. 2020. High-resolution structures of the SARS-CoV-2 2'-O-methyltransferase reveal strategies for structure-based inhibitor design. *Sci Signal* 13:eabe1202. <https://doi.org/10.1126/scisig.nal.abe1202>
56. Fernandez-Ballester G, Beltrao P, Gonzalez JM, Song Y-H, Wilmanns M, Valencia A, Serrano L. 2009. Structure-based prediction of the *Saccharomyces cerevisiae* SH3-ligand interactions. *J Mol Biol* 388:902–916. <https://doi.org/10.1016/j.jmb.2009.03.038>
57. Somovilla P, García-Crespo C, Martínez-González B, Soria ME, de Ávila AI, Gallego I, Mínguez P, Durán-Pastor A, Ferrer-Orta C, Salar-Vidal L, Esteban-Muñoz M, Zuñiga S, Sola I, Enjuanes L, Esteban J, Fernandez-Roblas R, Gadea I, Gómez J, Verdaguer N, Domingo E, Perales C. 2023. Atypical mutational spectrum of SARS-CoV-2 replicating in the presence of ribavirin. *Antimicrob Agents Chemother* 67:e0131522. <https://doi.org/10.1128/aac.01315-22>
58. Gregori J, Perales C, Rodríguez-Frias F, Esteban JI, Quer J, Domingo E. 2016. Viral quasiespecies complexity measures. *Virology (Auckl)* 493:227–237. <https://doi.org/10.1016/j.virol.2016.03.017>
59. Gregori J, Rodríguez-Frias F, Quer J. 2023. Viral quasiespecies diversity and evolution. A bioinformatics molecular approach
60. Chen J, Zhao Y, Sun Y. 2018. *De novo* haplotype reconstruction in viral quasiespecies using paired-end read guided path finding. *Bioinformatics* 34:2927–2935. <https://doi.org/10.1093/bioinformatics/bty202>
61. Wilm A, Aw PPK, Bertrand D, Yeo GHT, Ong SH, Wong CH, Khor CC, Petric R, Hibberd ML, Nagarajan N. 2012. LoFreq: a sequence-quality aware, ultra-sensitive variant caller for uncovering cell-population heterogeneity from high-throughput sequencing datasets. *Nucleic Acids Res* 40:11189–11201. <https://doi.org/10.1093/nar/gks918>
62. Agudo R, Arias A, Domingo E. 2009. 5-fluorouracil in lethal mutagenesis of foot-and-mouth disease virus. *Future Med Chem* 1:529–539. <https://doi.org/10.4155/fmc.09.26>
63. Sánchez-Jiménez C, Olivares I, de Ávila Lucas AI, Toledano V, Gutiérrez-Rivas M, Lorenzo-Redondo R, Grande-Pérez A, Domingo E, López-Galíndez C. 2012. Mutagen-mediated enhancement of HIV-1 replication in persistently infected cells. *Virology (Auckl)* 424:147–153. <https://doi.org/10.1016/j.virol.2011.12.016>
64. Shealy YF, Frye JL, DuBois NF, Shaddix SC, Brockman RW. 1981. Carbocyclic analogues of 5-fluorouracil nucleosides. *J Med Chem* 24:1083–1086. <https://doi.org/10.1021/jm00141a013>
65. Donaldson EF, Sims AC, Graham RL, Denison MR, Baric RS. 2007. Murine hepatitis virus replicase protein nsp10 is a critical regulator of viral RNA synthesis. *J Virol* 81:6356–6368. <https://doi.org/10.1128/JVI.02805-06>
66. Grimes SL, Heaton BE, Anderson ML, Burke K, Stevens L, Lu X, Heaton NS, Denison MR, Anderson-Daniels J. 2025. The coronavirus nsp14 exoribonuclease interface with the cofactor nsp10 is essential for efficient virus replication and enzymatic activity. *J Virol* 99:e0170824. <https://doi.org/10.1128/jvi.01708-24>
67. Subissi L, Posthuma CC, Collet A, Zevenhoven-Dobbe JC, Gorbalenya AE, Decroly E, Snijder EJ, Canard B, Imbert I. 2014. One severe acute respiratory syndrome coronavirus protein complex integrates processive RNA polymerase and exonuclease activities. *Proc Natl Acad Sci USA* 111:E3900–E3909. <https://doi.org/10.1073/pnas.1323705111>
68. Martínez-González B, Soria ME, Vázquez-Sirvent L, Ferrer-Orta C, Lobo-Vega R, Mínguez P, de la Fuente L, Llorens C, Soriano B, Ramos-Ruiz R, et al. 2022. SARS-CoV-2 mutant spectra at different depth levels reveal an overwhelming abundance of low frequency mutations. *Pathogens* 11:662. <https://doi.org/10.3390/pathogens11060662>
69. Martínez-González B, Soria ME, Vázquez-Sirvent L, Ferrer-Orta C, Lobo-Vega R, Mínguez P, de la Fuente L, Llorens C, Soriano B, Ramos R, et al. 2022. SARS-CoV-2 point mutation and deletion spectra and their association with different disease outcomes. *Microbiol Spectr* 10:e0022122. <https://doi.org/10.1128/spectrum.00221-22>
70. Matyášek R, Kovařík A. 2020. Mutation patterns of human SARS-CoV-2 and Bat RaTG13 coronavirus genomes are strongly biased towards C>U transitions, indicating rapid evolution in their hosts. *Genes (Basel)* 11:761. <https://doi.org/10.3390/genes11070761>
71. Yi K, Kim SY, Bleazard T, Kim T, Youk J, Ju YS. 2021. Mutational spectrum of SARS-CoV-2 during the global pandemic. *Exp Mol Med* 53:1229–1237. <https://doi.org/10.1038/s12276-021-00658-z>
72. Digard P, Lee HM, Sharp C, Grey F, Gaunt E. 2020. Intra-genome variability in the dinucleotide composition of SARS-CoV-2. *Virus Evol* 6:veaa057. <https://doi.org/10.1093/ve/veaa057>
73. Roy A, Guo F, Singh B, Gupta S, Paul K, Chen X, Sharma NR, Jaishee N, Irwin DM, Shen Y. 2021. Base composition and host adaptation of the SARS-CoV-2: insight from the codon usage perspective. *Front Microbiol* 12:548275. <https://doi.org/10.3389/fmicb.2021.548275>
74. Grande-Pérez A, Sierra S, Castro MG, Domingo E, Lowenstein PR. 2002. Molecular indeterminism in the transition to error catastrophe: systematic elimination of lymphocytic choriomeningitis virus through mutagenesis does not correlate linearly with large increases in mutant spectrum complexity. *Proc Natl Acad Sci USA* 99:12938–12943. <https://doi.org/10.1073/pnas.182426999>
75. Tilk S, Frydman J, Petrov D, Curtis C. 2023. Abstract LB075: Cancers adapt to their mutational load by buffering protein misfolding stress. *Cancer Res* 83:LB075–LB075. <https://doi.org/10.1158/1538-7445.AM2023-LB075>
76. Chen S, Liu Y, Zhang Y, Wierbowski SD, Lipkin SM, Wei X, Yu H. 2022. A full-proteome, interaction-specific characterization of mutational hotspots across human cancers. *Genome Res* 32:135–149. <https://doi.org/10.1101/gr.275437.121>
77. Mendez R, Fritsche M, Porto M, Bastolla U. 2010. Mutation bias favors protein folding stability in the evolution of small populations. *PLoS Comput Biol* 6:e1000767. <https://doi.org/10.1371/journal.pcbi.1000767>
78. Xiong D, Lee D, Li L, Zhao Q, Yu H. 2022. Implications of disease-related mutations at protein–protein interfaces. *Curr Opin Struct Biol* 72:219–225. <https://doi.org/10.1016/j.sbi.2021.11.012>
79. Bloom JD, Neher RA. 2023. Fitness effects of mutations to SARS-CoV-2 proteins. *Virus Evol* 9:vead055. <https://doi.org/10.1093/ve/vead055>
80. Hensel Z. 2025. Secondary structure of the SARS-CoV-2 genome is predictive of nucleotide substitution frequency. *eLife* 13:RP98102. <https://doi.org/10.7554/eLife.98102>
81. Symons J, Chung C, Verheijen BM, Shemtov SJ, de Jong D, Amatngalim G, Nijhuis M, Vermulst M, Gout J-F. 2025. The mutational landscape of SARS-CoV-2 provides new insight into viral evolution and fitness. *Nat Commun* 16:6425. <https://doi.org/10.1038/s41467-025-61555-x>
82. Lo-Man R, Langeveld JPM, Martineau P, Hofnung M, Melloen RH, Leclerc C. 1998. Immunodominance does not result from peptide competition for MHC class II presentation. *J Immunol* 160:1759–1766. <https://doi.org/10.4049/jimmunol.160.4.1759>
83. Vilas Boas LCP, Campos ML, Berlanda RLA, de Carvalho Neves N, Franco OL. 2019. Antiviral peptides as promising therapeutic drugs. *Cell Mol Life Sci* 76:3525–3542. <https://doi.org/10.1007/s00018-019-03138-w>
84. Zhao H, To KKW, Lam H, Zhou X, Chan J-W, Peng Z, Lee ACY, Cai J, Chan W-M, Ip JD, Chan C-S, Yeung ML, Zhang AJ, Chu AWH, Jiang S, Yuen K-Y. 2021. Cross-linking peptide and repurposed drugs inhibit both entry pathways of SARS-CoV-2. *Nat Commun* 12:1517. <https://doi.org/10.1038/s41467-021-21825-w>
85. Ogando NS, El Kazzi P, Zevenhoven-Dobbe JC, Bontes BW, Decombe A, Posthuma CC, Thiel V, Canard B, Ferron F, Decroly E, Snijder EJ. 2021. Structure–function analysis of the nsp14 N7–guanine methyltransferase reveals an essential role in *Betacoronavirus* replication. *Proc Natl*

- Acad Sci USA 118:e2108709118. <https://doi.org/10.1073/pnas.2108709118>
86. Al Musaimi O, Lombardi L, Williams DR, Albericio F. 2022. Strategies for improving peptide stability and delivery. *Pharmaceuticals (Basel)* 15:1283. <https://doi.org/10.3390/ph15101283>
 87. Nada H, Choi Y, Kim S, Jeong KS, Meanwell NA, Lee K. 2024. New insights into protein–protein interaction modulators in drug discovery and therapeutic advance. *Signal Transduct Target Ther* 9:341. <https://doi.org/10.1038/s41392-024-02036-3>
 88. Takechi-Haraya Y, Ohgita T, Kotani M, Kono H, Saito C, Tamagaki-Asahina H, Nishitsuji K, Uchimura K, Sato T, Kawano R, Sakai-Kato K, Izutsu K-I, Saito H. 2022. Effect of hydrophobic moment on membrane interaction and cell penetration of apolipoprotein E-derived arginine-rich amphipathic α -helical peptides. *Sci Rep* 12:4959. <https://doi.org/10.1038/s41598-022-08876-9>
 89. Liu R, Liu Z, Peng H, Lv Y, Feng Y, Kang J, Lu N, Ma R, Hou S, Sun W, Ying Q, Wang F, Gao Q, Zhao P, Zhu C, Wang Y, Wu X. 2022. Bomidin: an optimized antimicrobial peptide with broad antiviral activity against enveloped viruses. *Front Immunol* 13. <https://doi.org/10.3389/fimmu.2022.851642>
 90. Skalickova S, Heger Z, Krejcová L, Pekarik V, Bastl K, Janda J, Kostolansky F, Vareckova E, Zitka O, Adam V, Kizek R. 2015. Perspective of use of antiviral peptides against influenza virus. *Viruses* 7:5428–5442. <https://doi.org/10.3390/v7102883>
 91. Eberle RJ, Gering I, Tusche M, Ostermann PN, Müller L, Adams O, Schaal H, Olivier DS, Amaral MS, Arni RK, Willbold D, Coronado MA. 2022. Design of D-amino acids SARS-CoV-2 main protease inhibitors using the cationic peptide from rattlesnake venom as a scaffold. *Pharmaceuticals (Basel)* 15:540. <https://doi.org/10.3390/ph15050540>
 92. Neumann K, Farnung J, Baldauf S, Bode JW. 2020. Prevention of aspartimide formation during peptide synthesis using cyanosulfurylides as carboxylic acid-protecting groups. *Nat Commun* 11:982. <https://doi.org/10.1038/s41467-020-14755-6>
 93. Kumar S, Stecher G, Li M, Knyaz C, Tamura K. 2018. MEGA X: molecular evolutionary genetics analysis across computing platforms. *Mol Biol Evol* 35:1547–1549. <https://doi.org/10.1093/molbev/msy096>
 94. Madani F, Lindberg S, Langel U, Futaki S, Gräslund A. 2011. Mechanisms of cellular uptake of cell-penetrating peptides. *J Biophys* 2011:414729. <https://doi.org/10.1155/2011/414729>
 95. Barnard DL, Hubbard VD, Smee DF, Sidwell RW, Watson KGW, Tucker SPT, Reece PAR. 2004. *In vitro* activity of expanded-spectrum pyridazinyl oxime ethers related to pirodavir: novel capsid-binding inhibitors with potent antipicornavirus activity. *Antimicrob Agents Chemother* 48:1766–1772. <https://doi.org/10.1128/AAC.48.5.1766-1772.2004>
 96. Zhao J, Guo S, Yi D, Li Q, Ma L, Zhang Y, Wang J, Li X, Guo F, Lin R, Liang C, Liu Z, Cen S. 2021. A cell-based assay to discover inhibitors of SARS-CoV-2 RNA dependent RNA polymerase. *Antiviral Res* 190:105078. <https://doi.org/10.1016/j.antiviral.2021.105078>
 97. Zhou S, Hill CS, Sarkar S, Tse LV, Woodburn BMD, Schinazi RF, Sheahan TP, Baric RS, Heise MT, Swanstrom R. 2021. β -D-N³-hydroxycytidine Inhibits SARS-CoV-2 through lethal mutagenesis but is also mutagenic to mammalian cells. *J Infect Dis* 224:415–419. <https://doi.org/10.1093/infdis/jiab247>
 98. Liu C, Shi W, Becker ST, Schatz DG, Liu B, Yang Y. 2021. Structural basis of mismatch recognition by a SARS-CoV-2 proofreading enzyme. *Science* 373:1142–1146. <https://doi.org/10.1126/science.abi9310>
 99. Moeller NH, Shi K, Demir Ö, Belica C, Banerjee S, Yin L, Durfee C, Amaro RE, Aihara H. 2022. Structure and dynamics of SARS-CoV-2 proofreading exonuclease ExoN. *Proc Natl Acad Sci USA* 119:e2106379119. <https://doi.org/10.1073/pnas.2106379119>
 100. Amicone M, Borges V, Alves MJ, Isidro J, Zé-Zé L, Duarte S, Vieira L, Guiomar R, Gomes J, Gordo I. 2022. Mutation rate of SARS-CoV-2 and emergence of mutators during experimental evolution. *Evol Med Public Health* 10:142–155. <https://doi.org/10.1093/emph/eoac010>
 101. Eckerle LD, Becker MM, Halpin RA, Li K, Venter E, Lu X, Scherbakova S, Graham RL, Baric RS, Stockwell TB, Spiro DJ, Denison MR. 2010. Infidelity of SARS-CoV Nsp14-exonuclease mutant virus replication is revealed by complete genome sequencing. *PLoS Pathog* 6:e1000896. <https://doi.org/10.1371/journal.ppat.1000896>
 102. Bobrowski T, Chen L, Eastman RT, Itkin Z, Shinn P, Chen CZ, Guo H, Zheng W, Michael S, Simeonov A, Hall MD, Zakharov AV, Muratov EN. 2021. Synergistic and antagonistic drug combinations against SARS-CoV-2. *Mol Ther* 29:873–885. <https://doi.org/10.1016/j.jymthe.2020.12.016>
 103. Gidari A, Sabbatini S, Schiaroli E, Bastianelli S, Pierucci S, Busti C, Saraca LM, Capogrossi L, Pasticci MB, Francisci D. 2023. Synergistic activity of remdesivir–nirmatrelvir combination on a SARS-CoV-2 *in vitro* model and a case report. *Viruses* 15:1577. <https://doi.org/10.3390/v15071577>
 104. Melville K, Rodriguez T, Dobrovolsky HM. 2018. Investigating different mechanisms of action in combination therapy for influenza. *Front Pharmacol* 9:1207. <https://doi.org/10.3389/fphar.2018.01207>
 105. Tang W-F, Chang Y-H, Lin C-C, Jheng J-R, Hsieh C-F, Chin Y-F, Chang T-Y, Lee J-C, Liang P-H, Lin C-Y, et al. 2024. BPR3P0128, a non-nucleoside RNA-dependent RNA polymerase inhibitor, inhibits SARS-CoV-2 variants of concern and exerts synergistic antiviral activity in combination with remdesivir. *Antimicrob Agents Chemother* 68:e0095623. <https://doi.org/10.1128/aac.00956-23>
 106. Wagoner J, Herring S, Hsiang T-Y, Ianevski A, Biering SB, Xu S, Hoffmann M, Pöhlmann S, Gale M, Aittokallio T, Schiffer JT, White JM, Polyak SJ. 2022. Combinations of host- and virus-targeting antiviral drugs confer synergistic suppression of SARS-CoV-2. *Microbiol Spectr* 10:e0333122. <https://doi.org/10.1128/spectrum.03331-22>
 107. Casas AI, Hassan AA, Larsen SJ, Gomez-Rangel V, Elbatreek M, Kleikers PWM, Guney E, Egea J, López MG, Baumbach J, Schmidt H. 2019. From single drug targets to synergistic network pharmacology in ischemic stroke. *Proc Natl Acad Sci USA* 116:7129–7136. <https://doi.org/10.1073/pnas.1820799116>
 108. Ianevski A, Yao R, Zusinaite E, Lello LS, Wang S, Jo E, Yang J, Ravlo E, Wang W, Lysvand H, et al. 2021. Synergistic interferon-alpha-based combinations for treatment of SARS-CoV-2 and other viral infections. *Viruses* 13:2489. <https://doi.org/10.3390/v13122489>
 109. Yang M, Jaaks P, Dry J, Garnett M, Menden MP, Saez-Rodriguez J. 2020. Stratification and prediction of drug synergy based on target functional similarity. *npj Syst Biol Appl* 6:1–10. <https://doi.org/10.1038/s41540-020-0136-x>
 110. Woodall M, Ellis S, Zhang S, Kembou-Ringert J, Kite K-A, Buggiotti L, Jacobs AI, Agyeman AA, Masonou T, Palor M, McHugh TD, Breuer J, Standing JF, Smith CM. 2025. Efficient *in vitro* assay for evaluating drug efficacy and synergy against emerging SARS-CoV-2 strains. *Antimicrob Agents Chemother* 69:e0123324. <https://doi.org/10.1128/aac.01233-24>
 111. Grande-Pérez A, Lázaro E, Lowenstein P, Domingo E, Manrubia SC. 2005. Suppression of viral infectivity through lethal defection. *Proc Natl Acad Sci USA* 102:4448–4452. <https://doi.org/10.1073/pnas.0408871102>
 112. Ortega-Prieto AM, Sheldon J, Grande-Pérez A, Tejero H, Gregori J, Quer J, Esteban JI, Domingo E, Perales C. 2013. Extinction of hepatitis C virus by ribavirin in hepatoma cells involves lethal mutagenesis. *PLoS One* 8:e71039. <https://doi.org/10.1371/journal.pone.0071039>
 113. Perales C, Iranzo J, Manrubia SC, Domingo E. 2012. The impact of quasispecies dynamics on the use of therapeutics. *Trends Microbiol* 20:595–603. <https://doi.org/10.1016/j.tim.2012.08.010>
 114. Becares M, Pascual-Iglesias A, Nogales A, Sola I, Enjuanes L, Zuñiga S. 2016. Mutagenesis of coronavirus nsp14 reveals its potential role in modulation of the innate immune response. *J Virol* 90:5399–5414. <https://doi.org/10.1128/JVI.03259-15>
 115. Dragoni F, Kwaa AK, Traut CC, Veenhuis RT, Woldemeskel BA, Camilo-Contreras A, Raymond HE, Dykema AG, Scully EP, Rosecrans AM, Smith KN, Bushman FD, Simonetti FR, Blankson JN. 2023. Proviral location affects cognate peptide–induced virus production and immune recognition of HIV-1–infected T cell clones. *J Clin Invest* 133:e171097. <https://doi.org/10.1172/JCI171097>
 116. Lee Y-CJ, Shirkey JD, Park J, Bisht K, Cowan AJ. 2022. An overview of antiviral peptides and rational bidesign considerations. *Biodes Res* 2022:9898241. <https://doi.org/10.34133/2022/9898241>
 117. Tague EP, McMahan JB, Tague N, Dunlop MJ, Ngo JT. 2023. Controlled protein activities with viral proteases, antiviral peptides, and antiviral drugs. *ACS Chem Biol* 18:1228–1236. <https://doi.org/10.1021/acscchembio.3c00138>
 118. Hu Y, Lewandowski EM, Tan H, Zhang X, Morgan RT, Zhang X, Jacobs LMC, Butler SG, Gongora MV, Choy J, Deng X, Chen Y, Wang J. 2023. Naturally occurring mutations of SARS-CoV-2 main protease confer drug resistance to nirmatrelvir. *ACS Cent Sci* 9:1658–1669. <https://doi.org/10.1021/acscentsci.3c00538>
 119. Tan H, Zhang Q, Georgiou K, Zhang S, Li K, Lambrinidis G, Kolocouris A, Deng X, Wang J. 2025. Identification of naturally occurring drug-resistant mutations of SARS-CoV-2 papain-like protease. *Nat Commun* 16:4548. <https://doi.org/10.1038/s41467-025-59922-9>

120. Chang L-J, Chen T-H. 2021. NSP16 2'-O-MTase in coronavirus pathogenesis: possible prevention and treatments strategies. *Viruses* 13:538. <https://doi.org/10.3390/v13040538>
121. Vom Hemdt A, Thienel AL, Ciupka K, Wieseler J, Proksch HM, Schlee M, Kümmerer BM. 2024. 2'-O-methyltransferase-deficient yellow fever virus: restricted replication in the midgut and secondary tissues of *Aedes aegypti* mosquitoes severely limits dissemination. *PLoS Pathog* 20:e1012607. <https://doi.org/10.1371/journal.ppat.1012607>
122. Schindewolf C, Menachery VD. 2023. Coronavirus 2'-O-methyltransferase: a promising therapeutic target. *Virus Res* 336:199211. <https://doi.org/10.1016/j.virusres.2023.199211>
123. Johnson KA, Dangerfield T. 2021. Mechanisms of inhibition of viral RNA replication by nucleotide analogs. *Enzymes* 49:39–62. <https://doi.org/10.1016/bs.enz.2021.07.001>
124. Moreno H, Tejero H, de la Torre JC, Domingo E, Martín V. 2012. Mutagenesis-mediated virus extinction: virus-dependent effect of viral load on sensitivity to lethal defection. *PLoS One* 7:e32550. <https://doi.org/10.1371/journal.pone.0032550>
125. Perales C, Agudo R, Manrubia SC, Domingo E. 2011. Influence of mutagenesis and viral load on the sustained low-level replication of an RNA virus. *J Mol Biol* 407:60–78. <https://doi.org/10.1016/j.jmb.2011.01.026>
126. Sardanyés J, Elena SF. 2011. Quasispecies spatial models for RNA viruses with different replication modes and infection strategies. *PLoS One* 6:e24884. <https://doi.org/10.1371/journal.pone.0024884>
127. Tapia N, Fernández G, Parera M, Gómez-Mariano G, Clotet B, Quiñones-Mateu M, Domingo E, Martínez MA. 2005. Combination of a mutagenic agent with a reverse transcriptase inhibitor results in systematic inhibition of HIV-1 infection. *Virology (Auckl)* 338:1–8. <https://doi.org/10.1016/j.virol.2005.05.008>
128. Domingo E, García-Crespo C, Soria ME, Perales C. 2023. Viral fitness, population complexity, host interactions, and resistance to antiviral agents. *Curr Top Microbiol Immunol* 439:197–235. https://doi.org/10.1007/978-3-031-15640-3_6
129. Gallego I, Gregori J, Soria ME, García-Crespo C, García-Álvarez M, Gómez-González A, Valiergue R, Gómez J, Esteban JI, Quer J, Domingo E, Perales C. 2018. Resistance of high fitness hepatitis C virus to lethal mutagenesis. *Virology (Auckl)* 523:100–109. <https://doi.org/10.1016/j.virol.2018.07.030>
130. Sheldon J, Beach NM, Moreno E, Gallego I, Piñeiro D, Martínez-Salas E, Gregori J, Quer J, Esteban JI, Rice CM, Domingo E, Perales C. 2014. Increased replicative fitness can lead to decreased drug sensitivity of hepatitis C virus. *J Virol* 88:12098–12111. <https://doi.org/10.1128/JVI.01860-14>
131. Penrice-Randal R, Bentley EG, Sharma P, Kirby A, Donovan-Banfield I, Kipar A, Mega DF, Bramwell C, Sharp J, Owen A, Hiscox JA, Stewart JP. 2025. The effect of molnupiravir and nirmatrelvir on SARS-CoV-2 genome diversity in severe models of COVID-19. *Microbiol Spectr* 13:e0182924. <https://doi.org/10.1128/spectrum.01829-24>
132. Shannon A, Selisko B, Le N-T-T, Huchting J, Touret F, Piorkowski G, Fattorini V, Ferron F, Decroly E, Meier C, Coutard B, Peersen O, Canard B. 2020. Rapid incorporation of Favipiravir by the fast and permissive viral RNA polymerase complex results in SARS-CoV-2 lethal mutagenesis. *Nat Commun* 11:4682. <https://doi.org/10.1038/s41467-020-18463-z>
133. Yin X, Popa H, Stapon A, Bouda E, Garcia-Diaz M. 2023. Fidelity of ribonucleotide incorporation by the SARS-CoV-2 replication complex. *J Mol Biol* 435:167973. <https://doi.org/10.1016/j.jmb.2023.167973>
134. Russ A, Wittmann S, Tsukamoto Y, Herrmann A, Deutschmann J, Lagisquet J, Ensser A, Kato H, Gramberg T. 2022. Nsp16 shields SARS-CoV-2 from efficient MDA5 sensing and IFIT1-mediated restriction. *EMBO Rep* 23:e55648. <https://doi.org/10.15252/embr.202255648>
135. Schindewolf C, Lokugamage K, Vu MN, Johnson BA, Scharton D, Plante JA, Kalveram B, Crocquet-Valdes PA, Sotcheff S, Jaworski E, Alvarado RE, Debbink K, Daugherty MD, Weaver SC, Routh AL, Walker DH, Plante KS, Menachery VD. 2023. SARS-CoV-2 uses nonstructural protein 16 to evade restriction by IFIT1 and IFIT3. *J Virol* 97:e0153222. <https://doi.org/10.1128/jvi.01532-22>
136. Lokugamage KG, Hage A, de Vries M, Valero-Jimenez AM, Schindewolf C, Dittmann M, Rajsbaum R, Menachery VD. 2020. Type I interferon susceptibility distinguishes SARS-CoV-2 from SARS-CoV. *J Virol* 94:e01410-20. <https://doi.org/10.1128/JVI.01410-20>
137. Prescott J, Hall P, Acuna-Retamar M, Ye C, Wathelet MG, Ebihara H, Feldmann H, Hjelle B. 2010. New world hantaviruses activate IFN λ production in type I IFN-deficient vero E6 cells. *PLoS One* 5:e11159. <https://doi.org/10.1371/journal.pone.0011159>
138. Sun D, Shi H, Guo D, Chen J, Shi D, Zhu Q, Zhang X, Feng L. 2015. Analysis of protein expression changes of the Vero E6 cells infected with classic PEDV strain CV777 by using quantitative proteomic technique. *J Virol Methods* 218:27–39. <https://doi.org/10.1016/j.jviromet.2015.03.002>
139. Salgado-Benavente C, Tas A, Zevenhoven-Dobbe JC, van der Meer Y, Sidorov IA, Leijts AA, Wanninger P, Gelderloos AT, van Kasteren PB, Snijder EJ, van Hemert MJ. 2024. Characterization of SARS-CoV-2 replication in human H1299/ACE2 cells: a versatile and practical infection model for antiviral research and beyond. *Antiviral Res* 227:105903. <https://doi.org/10.1016/j.antiviral.2024.105903>
140. Forni D, Pozzoli U, Cagliani R, Clerici M, Sironi M. 2023. Dinucleotide biases in RNA viruses that infect vertebrates or invertebrates. *Microbiol Spectr* 11:e0252923. <https://doi.org/10.1128/spectrum.02529-23>